Probing Structure and Reactivity of Metal Centers in Metal–Organic Frameworks by XAS Techniques

Probing structure and reactivity of metal centers in metal-organic frameworks by XAS techniques

Elisa Borfecchia,[1] Luca Braglia,[1,2] Francesca Bonino,[1] Silvia Bordiga,[1] Sigurd Øien,[3] Unni Olsbye,[3] Karl Petter Lillerud,[3] Jeroen A. van Bokhoven,[4,5] Kirill A. Lomachenko,[1,2] Alexander A. Guda,[2] Mikhail A. Soldatov,[2] Carlo Lamberti[2,6,*]

[1] Department of Chemistry, NIS and INSTM Reference Centers, University of Torino, Via Quarello 15, I-10135, Torino, Italy.
[2] Southern Federal University, Zorge Street 5, 344090 Rostov-on-Don, Russia.
[3] inGAP Centre for Research Based Innovation, Department of Chemistry, University of Oslo, P.O. Box 1033, N-0315 Oslo, Norway.
[4] Institute for Chemical and Bioengineering, ETH Zürich, CH-8093 Zurich, Switzerland
[5] Swiss Light Source, Paul Scherrer Institute, CH-5232 Villigen PSI, Switzerland
[6] Department of Chemistry, CrisDi Centre for crystallography, University of Torino, Via Giuria 7, I-10125 Torino, Italy. E-mail: carlo.lambeti@unito.it

Abstract The nature and the potentialities of a new class of crystalline porous materials (MOFs) are briefly discussed in the first part of this chapter. Successively, A selection of relevant results appearing in the last five years follows, underlying the relevant role of both EXAFS and XANES in determining the structural and electronic configuration of metals centers inside MOFs frameworks is presented.

Keywords for the subject index: Metal Organic Frameworks; MOFs; coordination polymers; P-MOFs; porous materials; linker, material functionalization; molecular adsorption; XANES; EXAFS; DFT calculations; Einstein model; Einstein temperature; Einstein frequency; parametric refinement; ligand exchange reaction; XANES simulations; finite difference method; full-potential XANES simulations; FDMNES; muffin tin approximation; beyond the muffin tin approximation; ΔXANES;

1. Introduction: relevance and flexibility of MOFs materials

In the last decade, Metal Organic Frameworks (MOFs, also known as coordination polymers) represented a new emerging class of porous materials that have focused the interest of many research laboratories worldwide.[1-18]. MOFs diverge from some zeolites in important aspects.[19,20] Indeed, MOFs exhibit a much larger diversity and flexibility in composition (see below Figure 1 and Figure 2) and have less demanding topological constraints in the formation of the porous lattices. The enormous number of new MOF frameworks reported every year reflects this flexibility and the large interest for their potential applications.[21] Zeolites are strictly based on tetrahedral building units and their different topology are based on the possibility to make a finite number of secondary building units,[22] whereas the inorganic cornerstone in MOF topologies may be a single metal atom or a more or less complex cluster of coordinated metal atoms or extended inorganic sub-structures extending in one, two or three dimensions. According to the recent classification done by Tranchemontagne et al.[23] the coordination of the inorganic cornerstone may span the whole range from 3 up to 66.

Completely different frameworks can be obtained by keeping the same linker connectivity and changing the cornerstone geometry, see Figure 1a, or by fixing the cornerstone geometry and changing the linker connectivity see Figure 1b. On top of this, cornerstones can be connected using different type of organic linkers, giving rise to the synthesis of isoreticular frameworks such as e.g. the IRMOF-1/IRMOF-16[24] or the UiO-66/UiO-68[25-27] series, see Figure 1c.

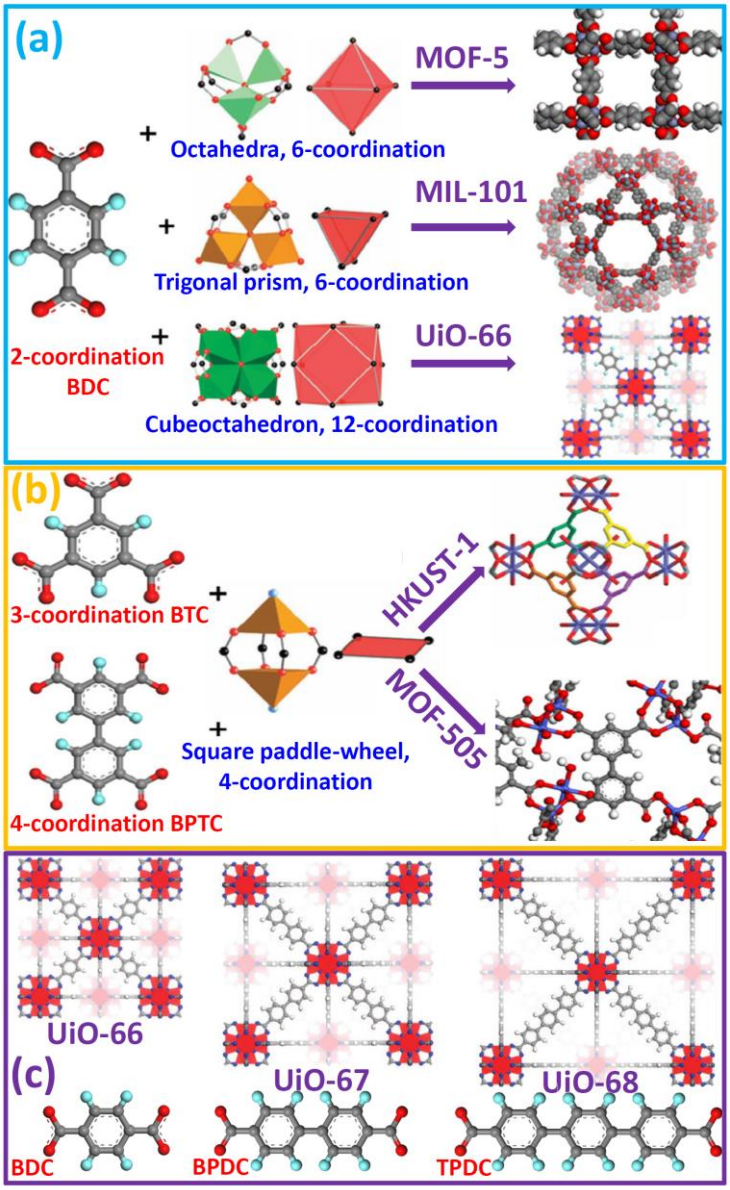

Figure 1. Examples of the flexibility in the construction of MOF structures. Part (a): fixing the linker connectivity (2-fold connected 1,4-benzene-dicarboxylate, (BDC)) and changing the cornerstone geometry. Part (b): fixing the cornerstone geometry and changing the linker connectivity (3-fold benzene-1,3,5-tricarboxilate (BTC) and 4-fold 3,3',5,5'-biphenyltetracarboxylate (BPTC)). Part (c): fixing both the linker connectivity (2-fold) the cornerstone geometry (12-fold coordinated cubeoctahedron), but changing the linker length BDC, 4,4′-biphenyl-dicarboxylate (BPDC) or 4,4′-terphenyl-dicarboxylate (TPDC). Adapted by permission of Springer (copyright 2010) from Ref. [28] (parts a,b) and of the American Chemical Society (copyright 2008) from Ref. [25] (part c).

Although the industrial application of MOFs is still limited to a few cases,[29,30] this new class of materials is foreseen to play an important role in the next future, in the fields of: (i) gas separation and purification in general,[31-34] and in particular: selective adsorption of H_2 or over N_2 or CO,[35] bulk separation of CO_2 under near-ambient conditions for the biogas upgrading,[36-39] selective capture of CO_2,[40-42] of CH_4,[40] or of for O_2,[43] hydrocarbons separation,[44] selective adsorption air purification of toxic chemicals,[45,46] enantioselective sorption of alcohols;[47] (ii) liquid phase separation;[33,48] (iii) adsorption and storage of gases;[49-54] (iv) materials for drug delivery;[55-58] (v) optical and luminescent materials;[59-67] (vi) photoactivable materials;[68] (vii) magnetic materials;[69,70] (viii) solid state ion conductors;[71] (ix) proton conductors;[72,73] (ix) materials for electronic and optoelectronic devices;[74] (x) materials for sensors;[67] (xi) catalysis

in general[28,75-79] and in particular for: enantioselective chiral reactions;[80-84] (xii) photocatalysis.[85,86]

As deeply described in several authoritative reviews and book chapters,[87-98] the functionalization of MOF materials remains one of the main challenges driving the MOF community, to make newer and newer structures, with specific functionalities. Indeed, the metal sites in most of the MOF structures show at maximum one coordination vacancy (and only after removal of the solvent, see the HKUST-1 and the CPO-27-Ni cases discussed in Sections 3.3 and 3.5, respectively), therefore limiting their application *e.g.* in catalysis, where at least two coordination vacancies are required.

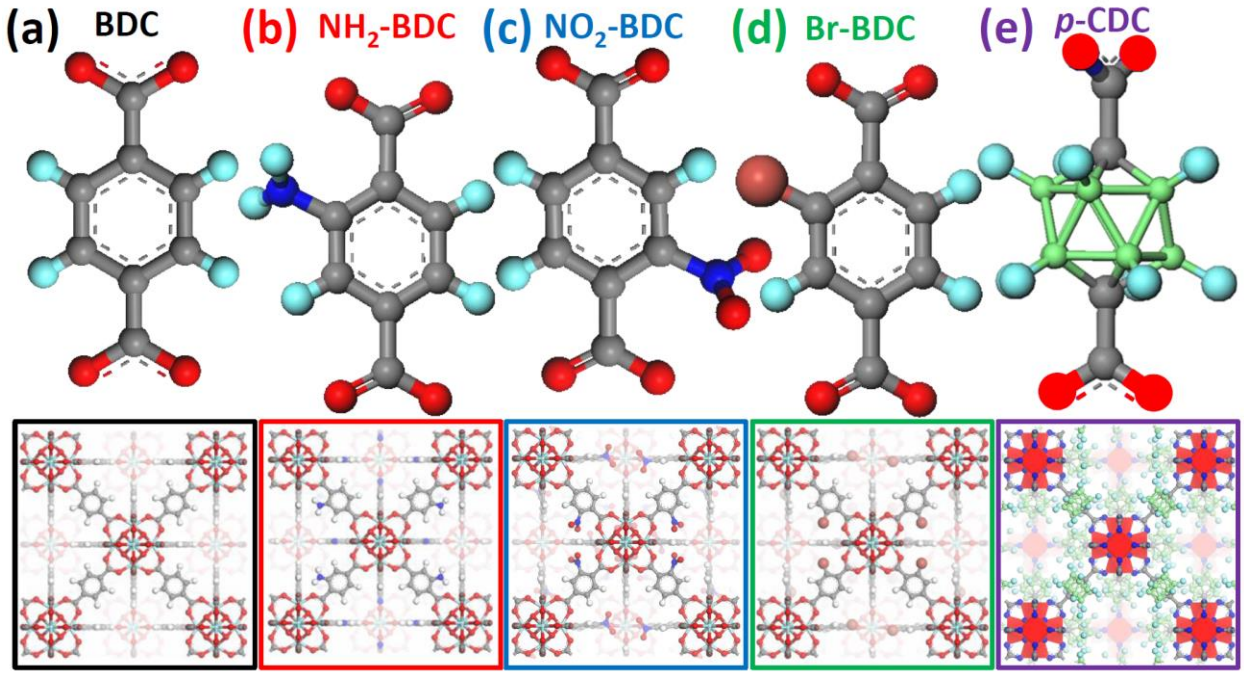

Figure 2. Examples of the flexibility in the linker functionalization of MOF structures: functionalized linker (top) and resulting MOF structure (bottom). Part (a): BDC linker, resulting in the standard UiO-66 framework. Part (b): NH_2-BDC linker. Part (c): NO_2-BDC linker. Part (d): Br-BDC linker. Part (e): *p*-carborane-dicarboxylate (*p*-CDC) linker. Top parts report the linkers, bottom parts report the insertion of the functionalized linker in the UiO-66 framework. Previously unpublished figure inspired from Refs. [28].

MOFs functionalization (see Figure 2 for some examples) has been performed following two main routes: (i) by using during the synthesis linkers containing functionalized groups[85,99-103] or by (ii) by performing post-synthesis modification of MOFs framework. The latter approach includes, e.g.: incorporating arenetricarbonyl complexes [$-C_6H_4M(CO)_3-$] (M = Cr, Mo) on the linkers by interaction with M-carbonyls;[104-106] performing click reaction between the azide groups in the MOF linker network and external alkynes[107,108] reduction of the aldehyde functionality of imidazolate-2-carboxyaldehyde linker by $NaBH_4$, to obtain the alcohol functionality and successive conversion to imine functionality by reaction with ethanolamine;[109] insertion in the linker of $-NH_2$ groups by interaction with nicotinoyl chloride[110] formation of $-NHCOCH_3$ or longer amide groups by interaction of $-NH_2$ groups with different acid anhydrides;[102,111,112] metalation reaction on N-containing organic linkers;[103,113] carboxy-functionalization;[114] amine-functionalization;[115,116] incapsulation of metal nanoparticles MOFs cavities.[117,118] In this chapter, examples of functionalized MOFs characterized by XAFS techniques are reported in Sections 3.2 (Pt-functionalized UiO-67) and 3.4 (phosphine functionalized MIL-101).

2. Relevance of XAS-techniques in understanding the structure and the reactivity of MOFs materials

The fact that MOFs are mainly constituted by low Z elements (C, O, N, H) implies that they are almost transparent to hard X-rays;[11,119-121] this allows to collect, at the metal K- or L-edges, high quality transmission X-ray absorption spectra characterized by an optimized edge jump $\Delta\mu x$ as high as 1.0-1.5, resulting in accurate data, analyzable up to 15-20 $Å^{-1}$. Figure 3a reports a clear example where high quality data collected up to high k values have been relevant in understanding fine structural details. The gray spectrum correspond to the k^3-weighted $\chi(k)$ of vacuum activated CPO-27-Ni MOF[122] (also known as MOF-74 or Ni_2(dhtp)) collected at 77 K. The blue spectrum has been recorded after N_2 dosage at 77 K.[123,124] Up to k ~ 11 $Å^{-1}$ the two spectra are almost undistinguishable. The small modification induced by the weak adsorption of N_2 molecule into the coordination vacancy of Ni^{2+} (Figure 3d) can be appreciated only in the 12-19 $Å^{-1}$ region. An accurate fit was performed in R-space (Figure 3b) resulting in a $Ni^{2+}\cdots N_2$ distance of 2.27 $\pm$ 0.03 Å. Interesting are also the small, but well defined changes observed in the XANES region (Figure 3c). See below Section 3.5 for an in depth discussion on the role of XANES simulations in understanding the adsorption geometries of CO and NO molecules on Ni^{2+} sites of CPO-27-Ni. EXAFS was used on the same CPO-27-Ni MOF system to define the coordination of CO (2.11 $\pm$ 0.02 Å),[125] H_2O (2.10 $\pm$ 0.04 Å)[126] and NO (1.87 $\pm$ 0.02 Å).[126]

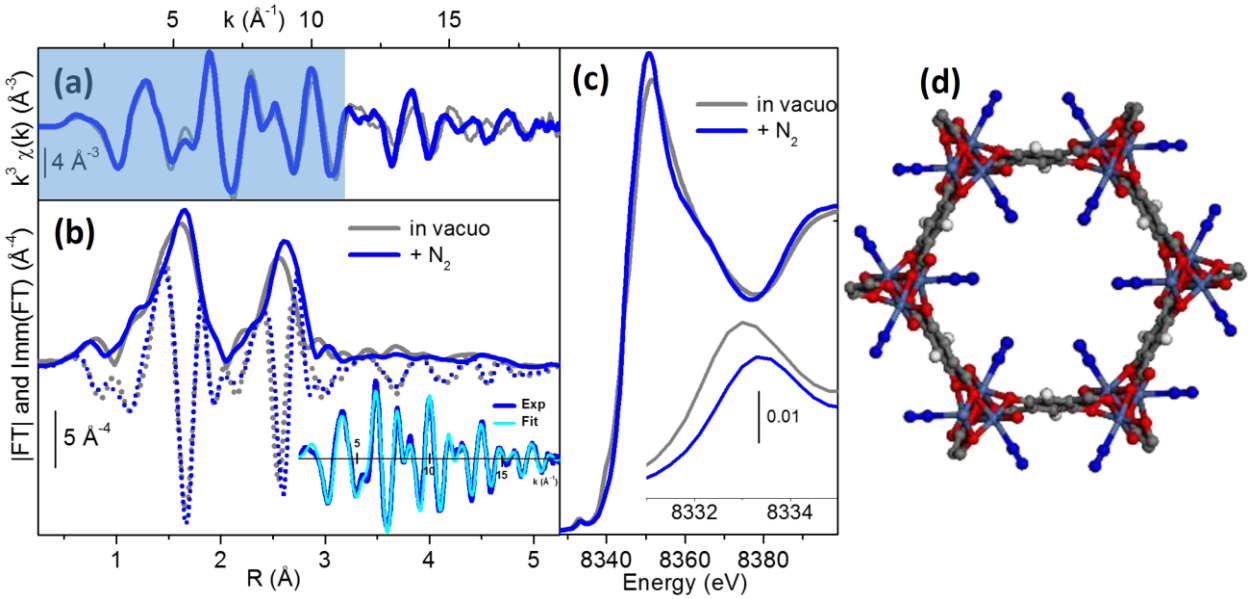

Figure 3. Part (a): EXAFS signals of CPO-27-Ni MOF, before (gray curve) and after (blue curve) N_2 adsorption at liquid nitrogen temperature (P_{N2} = 100 mbar) in k-space. A k^3-weight has been adopted. Part (b): phase uncorrected FT of the $k^3\chi(k)$ functions reported in part (a): modulus (full lines) and imaginary parts (dotted lines). Same color labelling as in part (a). Part (c): Normalized XANES spectra show the effect of N_2 dosage on CPO-27-Ni on the electronic levels of Ni. The inset reports a zoom on the dipole forbidden 1s $\rightarrow$ 3d electronic transition. Part (c):
Optimized periodic structures at B3LYP-D*/TZVP level of theory of CPO-27-Ni + N_2. View from the [001] direction. Parts (a-c) adapted with permission from Ref. [123], copyright Royal Society of Chemistry (2009); part (d) adapted with permission from Ref. [124] copyright Elsevier (2012).

The complementarity between long range order, investigated by diffraction techniques, and local range order, investigated by EXAFS, has already been recognized for complex systems, such as metalloproteins,[127,128] disordered mixed oxides,[129,130] ternary and quaternary semiconductor solid solutions[131,132] and will here be debated for MOFs. Actually, the chapter will have a wider view as it will deal with X-ray absorption spectroscopies, i.e. including both

EXAFS[133-136] and X-ray Absorption Near Edge Structure (XANES).[137-141]. Unfortunately, for space limitations, we will not consider X-ray emission spectroscopy (XES)[103,142-154] that has become in the last decade a very promising technique.

3. Selected recent examples

The role of XAS and related spectroscopies in understanding the structure and the reactivity of metal centers in metalorganic framework was reviewed by some of us in 2010.[11] In that critical review we report cases where EXAFS and XANES have been relevant in understanding the structural and electronic properties metal clusters in MOFs. In particular, materials with cluster corner stones (zero dimensional) and coordination four (HKUST-1, or $Cu_3(BTC)_2$),[155] six (MOF-5),[156] nine (Pt-Gd-MOF[100] and Pt-Y-MOF[99]) and twelve (UiO-66[25,26] and Ni-cubane[157]) as well as one example of MOF (CPO-27[123-126]) with a one dimensional inorganic backbone were discussed.

MOFs are crystalline materials with a complex structure (see above Figure 1 and Figure 2), consequently, very little information can be extracted from EXAFS data alone. To perform a complete EXAFS data analysis, able to reconstruct the whole inorganic cornerstone and its binding to the organic part, i.e. to reconstruct the local environment of a metal center up to 4-5 Å, a guessed 3D structure is mandatory. Usually the 3D structure comes from a diffraction study, but it may also come from ab initio optimization.[26,27] In review[11] it was shown that EXAFS can be successfully used in the following cases:

(i) To just confirm the structure obtained from X-ray or neutron powder diffraction refinements (hydroxylated UiO-66,[25,26] hydrated HKUST-1 [155], Ni-cubane [157] and as prepared Pt/Gd-[100] and Pt-Y-MOF ;[99] MOF)

(ii) To highlight that the inorganic cornerstone has a lower symmetry with respect to that of the organic framework, that escaped the diffraction refinement (dehydroxylated UiO-66);[25,26])

(iii) To obtain the local structure of the inorganic cluster in the desolvated material when desolvation causes a fragmentation of single crystals accompanied by a partial and reversible loss of long range ordering that causes peaks broadening, making impossible the structure solution from XRPD (dehydrated Pt/Gd-MOF)[100] or when simply the XRPD refinement (notwithstanding the quality of the collected pattern) does not reach a safe convergence (dehydrated HKUST-1);[155])

(iv) To obtain the local structure of the inorganic cluster in the desolvated material after coordination of a probe (or reactant) molecule, including cluster deformation upon molecule coordination and metal-molecule binding distance (HKUST-1[155] and CPO-27-Ni;[123-126,158]

(v) To highlight the presence of impurities in form of an amorphous extra-phase that escaped detection from diffraction methods (some MOF-5 synthesis).[156]

In review[11] it has also been underlined that, for points (iii) and (iv) the starting model to refine the EXAFS datum is that obtained from the refinement of the diffraction data collected on the solvated material after removal of the solvent molecule (iii) or after replacement of the solvent molecule by a probe molecule (iv). In the latter case the number of coordinated probe molecules as well as the adsorption geometry may be critical to be disclosed by EXAFS alone, because the scattering contribution from the probe molecule is usually a small fraction of the overall EXAFS signal, that is still dominated by the scattering of the ordered framework atoms. In these cases any help coming from independent techniques (IR, Raman, volumetric microcalorimetry, gravimetric adsorption etc…) is welcome to reduce the number of independent parameters optimized in the EXAFS data analysis. We will show in this chapter

(Section 3.5) the relevance of the use of accurate simulation of XANES to disclose the geometry and the stoichiometry of the metal site after adsorption.

On one hand it is evident that, beside point (i), EXAFS spectroscopy is a fundamental tool to disclose the local structure of the metal MOFs cornerstones. On the other hand, the existence of clear examples discussed in point (ii) and (v), where diffraction methods alone resulted in a wrong solution for the structure of the inorganic clusters, makes cases listed in point (i) not a trivial exercise but an important structural check, that is recommended for all new MOFs structures.

On top of this, related XANES (and possibly XES)[119,144,159,160] techniques provide complementary information on the metal electronic structure to complement standard UV-Vis, EPR measurements and ab initio calculations. In the following we will focus the attention of some relevant EXAFS and XANES results appeared in the literature in the last five years.

3.1. Zr UiO-66, 67 and Hf UiO-66 MOFs

The recently discovered UiO-66/67/68 class of isostructural MOFs[25] has attracted great interest because of its remarkable stability at high temperatures (up to 400 °C),[161] high pressures and in presence of different solvents acids and bases.[26] UiO-66 is obtained connecting $Zr_6O_4(OH)_4$ inorganic cornerstones with 1,4-benzene-dicarboxylate (BDC) as linker, while the isostructural UiO-67 material, obtained using the longer 4,4′ biphenyl-dicarboxylate (BPDC) linker[27] (Figure 1c) and Hf-UiO-66 is obtained keeping the UiO-66 linker (BDC) and substituting the $Zr_6O_4(OH)_4$ blocks with $Hf_6O_4(OH)_4$ corners.[162] Due to the rigidity of the framework several isostructural UiOs has been prepared and tasted for the stability and gas adsorption. Kandiah et al.[102] studied the thermal and chemical stabilities of isostructural UiO-66-X (X= NH_2, Br and NO_2, see Figure 2c,c,d) and observed the lower stability of this analogue with respect to parent UiO-66. Conversely, as documented by thermogravimetric studies UiO-67[27] and Hf-UiO-66[162] show thermal and chemical stability similar to that of UiO-66 and exhibit the expected surface area, as determined by low temperature volumetric N_2 adsorption isotherms. Such a high stability is related to the fact that each Zr-octahedron is 12-fold connected to adjacent octahedra. This connectivity is very common for metals, resulting in the highly packed fcc structure, but it is still almost unique in MOF topologies.[25]

All MOFs are synthesized in presence of a solvent, that has to be removed to make available the large pore volume for any practical applications. The desolvation process left almost unchanged the XRPD pattern of such materials:[25,27,162] besides a gain of intensity of the basal reflections (due to the removal of the electron density inside the pores)[163,164] all peaks remains in almost the same 2θ position with small intensity changes. Conversely, a huge modification of the EXAFS spectra is obtained in all cases, see Figure 4.

In the three hydroxylated materials, the structure determined from the Rietveld refinement of the XRPD corresponding patterns resulted in a straightforward interpretation of the complex EXAFS signals, see first three columns in Table 1. The dramatic modification undergone by the EXAFS spectrum upon dehydroxylation (see Figure 4) makes the data analysis not so straightforward. In the case of UiO-66 (see Figure 4b, but similar effects are observed in the two other cases) the changes are basically explained in terms of three main effects: (i) small contraction of the first M-O shell accompanied by a small decrease in coordination (erosion of the shoulder around 1.9 Å); (ii) relevant distortion of the second shell contribution showing a maximum that moves from 3.17 Å to 2.91 Å, with a shoulder at 3.41 Å, thus reflecting an important splitting of the R_{M1} distances of the octahedron sides; (iii) the almost complete disappearance of the weak contribution around 4.7 Å, due to the M-M SS signal of the octahedron diagonal (R_{M2}). For the three cases, differently to the hydroxylated cases, the 3D model obtained from the Rietveld refinement of XRPD data in the highly symmetric *Fm-3m* space group was inadequate to simulate the experimental datum. The origin of this failure was, obviously due to the inability of the model to account for two different R_{M1} and R_{M2} distances. For both UiO-66[26] and UiO-67[27] cases, the failure of the XRPD model was overcome by using the optimized geometry obtained by ab initio periodic calculations.

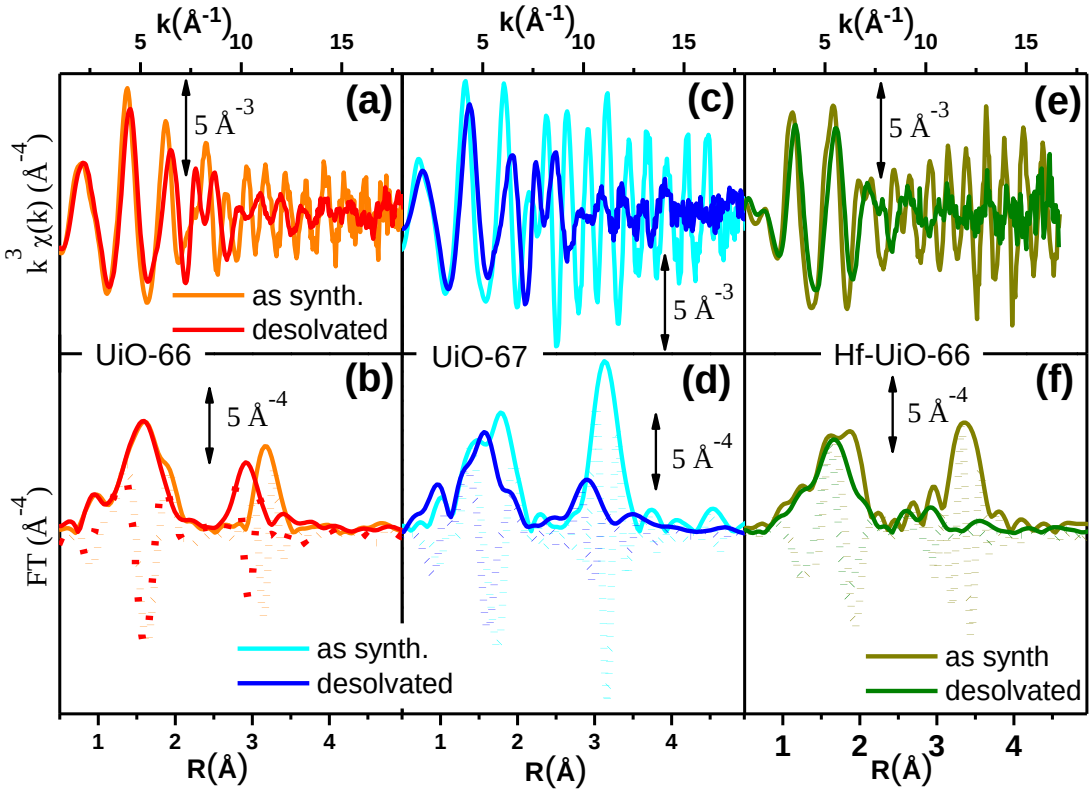

Figure 4. k- (top panels) and R-space (bottom panels) EXAFS data collected on UiO-66, UiO-67 and Hf-UiO-66, parts (a,b), (c,d) and (e,f), respectively. Both as synthesized (or hydroxylated) and desolvated (or dehydroxylated) forms of the three different isostructural MOFs have been measured. With the exception of desolvated Hf-UiO-66 sample (collected at 573 K) remaining spectra were collected at 300 K. Reproduced with permission from ref. [165].

The inorganic cornerstones of the as synthesized materials are perfect $M_6(OH)_4O_4$ octahedron (see model in Figure 5b), with 6 equivalent M at the vertex, 12 equivalent M-M1 sides and 3 equivalent and M-M2 diagonals. Upon desolvation two structural water molecules are lost per cornerstone unit (Figure 5a), that evolves from $M_6(OH)_4O_4$ to M_6O_6.[26,27,162] The new M_6O_6 octahedron compressed (2 opposite vertexes approaching, see model in Figure 5c) resulting in the shortening of 8 of the 12 edges, and the elongation of the other 4 edges. To take into account this variation we simulated the EXAFS contribution with two independently parameterized paths fixing for the degeneration a ratio of 1/3 and 2/3 with respect to the case of the single contribution.

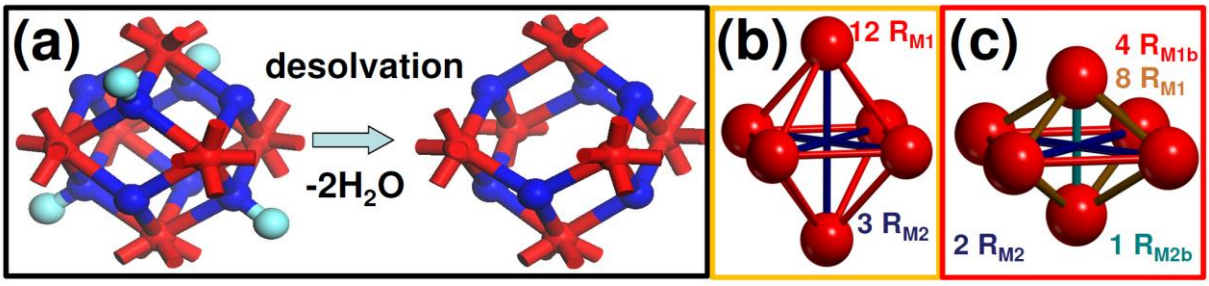

Figure 5. Part (a): Stick and ball representation of the dehydroxylation undergone by the inorganic $M_6O_4(OH)_4$ cornerstone upon thermal treatment at 300 °C in vacuo resulting in a distorted M_6O_6 cluster (M =Zr or Hf). Red, blue and cyan colors refer to M, O and H atoms, respectively. Part (b): Stick and ball representation of the perfect M_6 octahedron, showing 12 equivalent R_{M1} sides and 3 equivalent $R_{M2} = \sqrt{2}\ R_{M1}$ diagonals. Part (c): Stick and ball representation of a squeezed M_6 octahedron. The 12 sides are now split into 4 in-plane long M_{M1b} sides and 8 prismatic short M_{M1a} sides, while the 3 diagonals evolve into 2 in-plane long M_{M2b} and 1 orthogonal short M_{M2a} diagonals. For clarity, O atoms are omitted in parts (b) and (c). Reproduced with permission from ref. [165].

Table 1. Summary of the EXAFS refinement obtained on the hydroxylated and dehydroxylated forms of UiO-66,[26] UiO-67,[27] and Hf-UiO-66.[162] The EXAFS refinement of the hydroxylated materials was obtained using as input model the optimized structure from Rietveld refinement of the corresponding XRPD patterns. The EXAFS refinement of the dehydroxylated materials was obtained using as input model optimized *ab initio* calculations for the hydroxylated of UiO-66. With this approach the coordination number (N) of each contribution is fixed by the model stoichiometry. Refinement of the experimental amplitude is done by optimizing the overall amplitude factor S_0^2 only. The fitting of the higher shells was possible only adopting the axial compressed model of the M_6O_6 octahedron represented where eight octahedron sides R_{M1} are split into eight short prismatic distances (R_{M1}, N=8/3) and four long planar ones (R_{M1b}, N=4/3) and where the three diagonals R_{M2} are split into a short axial diagonal and (R_{M2a}, involving two M atoms out of six; N=1/3) and two long planar diagonals (R_{M2b}, involving four M atoms out of six; N=2/3). For the hydroxylated forms of UiO-66 and UiO-67 also the $R_{\mu3\text{-}O}$ and $R_{\mu3\text{-}OH}$ distances recently obtained by single crystal XRD have been reported for comparison. Adapted with permission from ref. [165].

	UiO-66	UiO-67	Hf-UiO-66	UiO-66	UiO-67	Hf-UiO-66
		hydroxylated			dehydroxylated	
T (K)	300	300	300	300	300	537
$R_{\mu3\text{-}O}$ (Å)	2.087 ± 0.008	2.12 ± 0.02	2.12 ± 0.01	2.06 ± 0.01	2.096 ± 0.007	2.06 ± 0.01
XRD $R_{\mu3\text{-}O}$ (Å)	2.064 ± 0.003	2.059 ± 0.002	-	-	-	-
R_{O1} & $R_{\mu3\text{-}OH}$ (Å)	2.235 ± 0.008	2.26 ± 0.01	2.25 ± 0.01	2.221 ± 0.007	2.249 ± 0.007	2.19 ± 0.01
XRD $R_{\mu3\text{-}OH}$ (Å)	2.254 ± 0.005	2.256 ± 0.008	-	-	-	-
R_C (Å)	3.19 ± 0.02	3.40 ± 0.06	3.23 ± 0.06	3.17 ± 0.04	3.15 ± 0.04)	3.22 ± 0.05
R_{M1} (Å)	3.511 ± 0.007	3.512 ± 0.006	3.510 ± 0.005	3.35 ± 0.01	3.365 ± 0.015	3.31 ± 0.03
R_{M1b} (Å)	-	-	-	3.74 ± 0.02	3.80 ± 0.03	3.45 ± 0.06
R_{M2} (Å)	4.99 ± 0.04	4.95 ± 0.03	4.964	4.14 ± 0.07)	4.15 ± 0.07	-
R_{M2b} (Å)	-	-	-	5.30 ± 0.04	5.46 ± 0.05	-

Summarizing, EXAFS spectroscopy allows to detect the evolution from $M_6(OH)_4O_4$ to M_6O_6 (M = Zr or Hf) of the inorganic cornerstones of UiO-66, UiO-67 and Hf-UiO-66 MOFs that escaped XRPD detection. DFT period calculations support EXAFS data. Only very recently, Øien et al.[166] succeeding in growing single crystals of UiO-66 and UiO-67 of sufficiently large size to allow synchrotron radiation single crystal data collection to be done. From such date it clearly emerges the presence of two different first shell μ_3 oxygen species, namely μ_3O and μ_3OH, which Zr–O distance agreed with the previous EXAFS studies,[26,27] see Table 1. These discrimination between first shell Zr neighbor escaped any previous XRPD analysis in all these class of materials, but was observed by EXAFS[26,27,162] and supported by IR spectroscopy.

3.2. Pt-functionalization of UiO-67 MOF

Introducing a chemically active Pt site as part of the UiO-67 framework is of great interest as platinum has rich redox chemistry, showing 0, II and IV stable oxidation states. Moreover, certain square planar Pt(II) coordination complexes are known to be active in C-H bond activation,[167-171] see the scheme reported in Figure 6a. In particular, the dichlorobipyrimidyl platinum(II), $PtCl_2$(BPYM), performs the catalytic oxidation in fuming or concentrated sulfuric acid, achieving high yields of methanol with selectivity higher than 90%.[172,173] It is consequently of potential interest to investigate the possibility to heterogenize such process anchoring the active Pt(II) complex on some high surface area material such as recently shown by the group of Schüth, for polymers first[174,175] and for N-doped carbons[176] successively.

Oien et al.[103] have recently succeeded in functionalizing UiO-67 with $PtCl_2(H_2BPDC)$ (Figure 6c) or $PtCl_4(H_2BPDC)$ units (Figure 6b), substituting 10% of the standard BPDC linkers. The authors used extended EXAFS and valence-to-core resonant inelastic X-ray scattering (RIXS) techniques to prove the insertion of Pt atoms in the expected framework position of UiO-67, see Figure 6c.

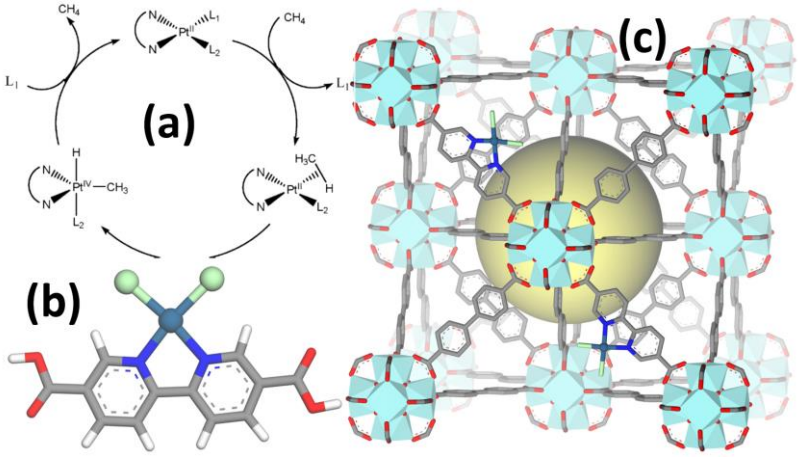

Figure 6. Part (a): Suggested catalytic cycle of the C–H activation on square planar Pt(II) complex. L_1, L_2 = movable ligands, such as Cl, as reported in parts (b,c). Part (b): structure of the isolated $H_2BPDCPtCl_2$ center inserted in the MOF structure showing 2 N and 2 Cl in the first coordination shell of Pt(II) and showing the distortion induced on the two rings by Pt insertion. Part (c) three-dimensional representation of Pt(II)-functionalized UiO-67 MOF. Part (a) adapted by permission of the American Chemical Society (copyright 2006) from Ref. [99]; parts (b) and (c) adapted by permission of the American Chemical Society (copyright 2015) from Ref. [103].

Using EXAFS and XANES, the structural and oxidation state of Pt can be monitored under *in situ* conditions. The elimination of chloride ligands from Pt in a continuous gas flow of H_2 have been monitored by EXAFS during temperature ramping, Figure 7a. The spectrum collected at room temperature (black curve) exhibits both the first shell Pt-N and the Pt-Cl contributions centered around 1.5 and 1.9 Å (phase uncorrected FT) highlighted by vertical blue and green dashed lines, respectively. Upon increasing the temperature both contributions decreases in intensity because of the increased Debye-Waller factors (σ^2_N and σ^2_{Cl}). Starting from about 600 K the Pt-Cl contribution shows a much more relevant decrease in temperature than the Pt-N one, suggesting that the system starts loosing chlorine ligands. A standard EXAFS analysis failed because of the high correlation between the coordination numbers ($N_{Pt–N}$; $N_{Pt–Cl}$) and the thermal parameters (σ^2_N; σ^2_{Cl}).[103] The problem was solved performing a complex data analysis briefly summarized hereafter.

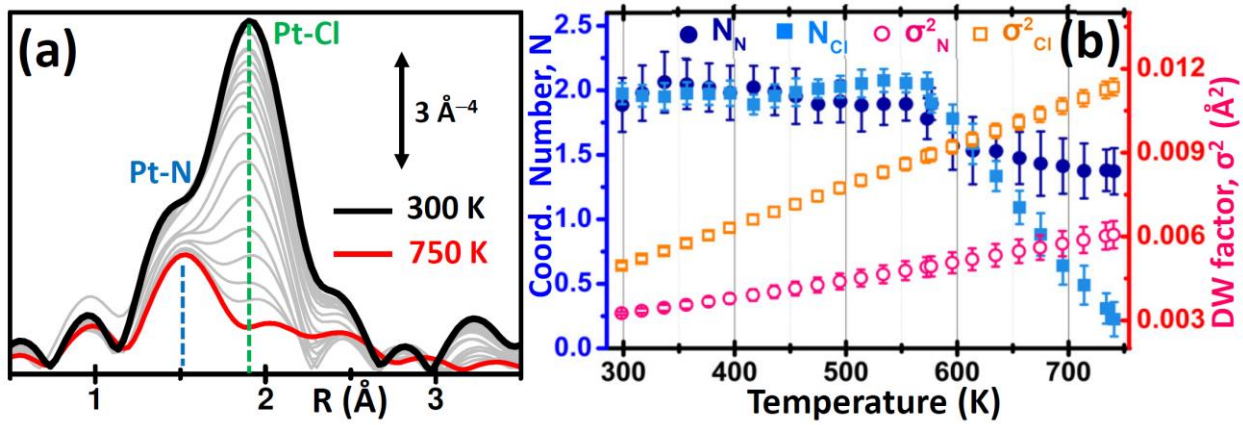

Figure 7. Part (a): k^3-weighted, phase uncorrected, FT of Pt L_3-edge EXAFS spectra collected during the operando H_2-TPR experiments on $PtCl_2(H_2BPYDC)$ functionalized UiO-67-Pt(II) MOF in the 300 K (black spectrum) – 750 K (red spectrum) range. Part (b): quantitative data analysis of the set of spectra shown in part (a) adopting a parametric refinement modeling the temperature dependence of the Debye-Waller factors (σ^2_N and σ^2_{Cl}) based on the Einstein model. Adapted by permission of the American Chemical Society (copyright 2015) from Ref. [103].

First authors worked only on the sub-set of data in the interval between RT and 473 K. In this temperature range no bond breaking occurs so that it was possible to fix $N_N = N_{Cl} = 2$. On

that sub-set they performed a parametric refinement, commonly adopted in XRPD Rietveld refinements,[164,177] adopting the Einstein model for describing the temperature dependence of both σ^2_N and σ^2_{Cl} factors. The Einstein model approximates the vibrational density of states as a Dirac delta function spiked at a single frequency named Einstein frequency (ω_E). The model assumes that the pairs Pt–N (or Pt–Cl) behaves as a quantum harmonic oscillator of mass equal to the reduced mass of the atomic pair (M = 13.070 and 30.004 amu for the Pt–N and Pt–Cl pairs, respectively). Under such assumptions, the $\sigma^2(T)$ behavior is straightforwardly determined by the only ω_E parameter according to the equation (1):[103,178]

$$\sigma^2(T) = \frac{\hbar}{M\omega_E} cotgh\left[\frac{\hbar\omega_E}{2k_BT}\right] = \frac{\hbar^2}{Mk_B\Theta_E} cotgh\left[\frac{\Theta_E}{2T}\right] \qquad (1)$$

Being Θ_E the Einstein temperature of the Pt–N (or Pt–Cl) bond, related to the Einstein frequency by the relationship: $\hbar\omega_E = k_B\Theta_E$, where $\hbar$ = 1.055 × 10^{-34} J s is the reduced Plank constant and k_B = 1.38 × 10^{-23} J K^{-1} is the Boltzmann constant.

This approach allowed the authors to reduce the number of parameters used to optimize the thermal factors of the series from ~40 to only two, Θ_E(Pt–N) and Θ_E(Pt–Cl), with a consequent reduction of the correlation among the optimized parameters and thus a reduction of the relative error bars. Once obtained the Einstein temperatures Θ_E(Pt–N) and Θ_E(Pt–Cl), the dependence of both σ^2_N and σ^2_{Cl} vs. T was straightforwardly obtained via Eq. (1) and extrapolated on the whole set of data (i.e. also above 473 °C). This strategy allowed to have stable fits on the whole temperature range while optimizing both N_N and N_{Cl}, as shown in Figure 7a. From this data analysis, it is evident that both N_N and N_{Cl} are stable to the stoichiometric values of 2.0 up to 575 K, when they start to decrease together. However, while N_{Cl} decreases almost linearly to 0.4 at 750 K, N_N undergoes a fast decrease to 1.6 at 610 K and then remains almost stable, being its value at 750 K of 1.4. This means that a prolonged activation in H_2 of the UiO-67-Pt(II)_PMLS MOF in the 610-640 K interval will result in a minimal loss of Pt(II), that will lose the Pt–N connection with the framework, but in the break of an important fraction of the Pt–Cl bonds. The experiment reported in Figure 7 proved that this activation temperature interval is ideal to obtain a material where most of the functionalized Pt(II) species are still linked to the MOF framework, exhibiting the coordination vacancies needed to make the UiO-67-Pt(II)_PMLS material a potential heterogeneous catalyst.[103] The presence of coordination vacancies at platinum sites was directly testified by IR spectroscopy of adsorbed CO.

EXAFS also provided evidence of the liquid phase ligand exchange with toluene-3,4-dithiol (H_2tdt) and of the liquid phase oxidative addition of Br_2 to Pt, see Figure 8. All observed reactions take place without any degradation of the framework, as testified by parallel XRPD experiments.

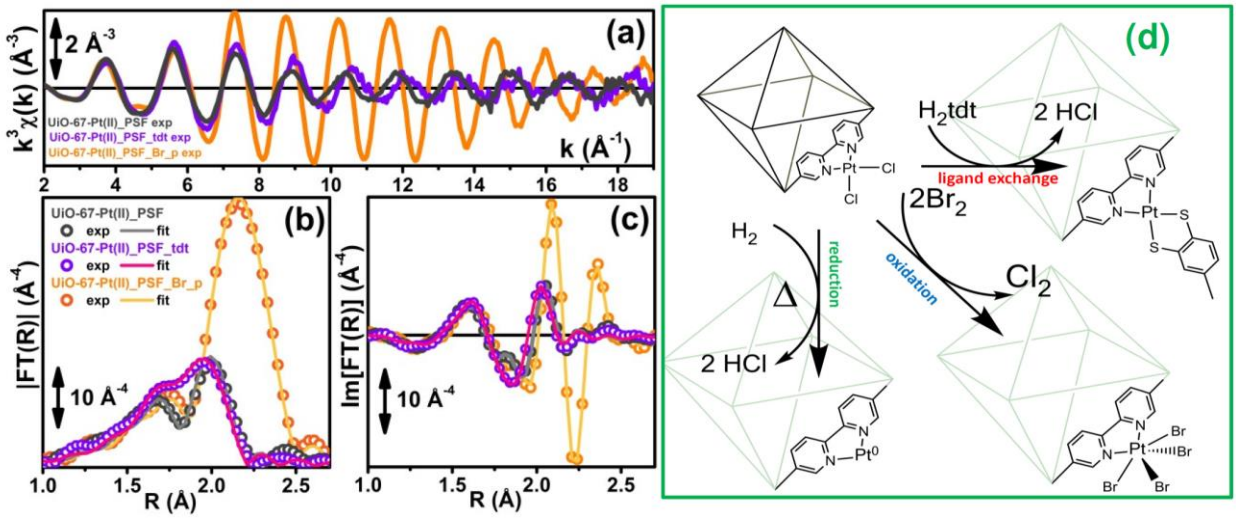

Figure 8. Part (a): experimental Pt L_3-edge $k^3\chi(k)$ spectra of UiO-67-Pt(II) before (black line) and after interaction with H_2tdt (violet line) and Br_2 (orange line). Part (b): modulus of the k^3-weighted, phase uncorrected FT of the experimental EXAFS spectra reported in part (a), open symbols, same color code as in part (a). Also reported, as continuous lines of similar color, are the corresponding best fits. Part (c): as part (b) for the imaginary parts of the k^3-weighted, phase uncorrected FT. Part (d): Schematic representation of the reactivity of Pt^{II} species in functionalized UiO-67-Pt MOFs that has been highlighted in the EXAFS and XANES study reported in Figure 7 and in parts (a-c) of this figure. The sketched square bi-pyramid represents the octahedral large cavity of UiO-67, measuring about 16 Å in diagonal.[25,27] Adapted by permission of the American Chemical Society (copyright 2015) from Ref. [103].

Also the XANES part of the XAS spectrum Figure 9a is sensitive to the changes undergone by the local environment of Pt(II) along the chemical reactions reported in Figure 8. Indeed, upon change in the Pt oxidation state, Pt L_3-edge XANES will show a very small edge shift while exhibit a noticeable variation of the intensity of the "white-line" peak.[103,179,180] Indeed, the XANES part of the Pt L_3-edge mainly promotes core $2p_{3/2}$ electrons into empty $5d_{3/2}$, $5d_{5/2}$ and 6s valence states, so manly probing the unoccupied density of 5d-states and partially 6s-states. The formal electronic configuration of platinum depends on its oxidation state as follows: Pt^0 ($6s^15d^9$), Pt^{II} ($6s^05d^8$) and Pt^{IV} ($6s^05d^6$); consequently an increase of the Pt oxidation states results in an higher density of unoccupied 5d states (and 6s) that is directly measured by an increase in the intensity of Pt L_3-edge. The XANES spectra reported in Figure 9a for UiO-67-Pt(II) MOF before (red line) and after interaction with H_2tdt (blue line) and Br_2 (green line) clearly follow this quantitative, phenomenological guiding line. Interaction with H_2tdt (blue spectrum in Figure 9a) does not change the white line intensity, affecting only the post edge and EXAFS region of the spectrum; on these basis it was concluded that we are a ligand exchange reaction occurred. Conversely interaction with Br_2 (green spectrum in Figure 9a) results in a significant increase in the white line intensity, testifying an oxidation process from Pt(II) to Pt(IV).[103]

On a more quantitative ground, the simulation of the XANES spectra, performed with ADF code ADF code on the H_2bpydcPtCl_2, H_2bpydcPt-tdt and H_2bpydcPtBr_4 molecular fragments (Figure 9b), were able to reproduce correctly the variation of the white line intensity, and post edge features.[181]

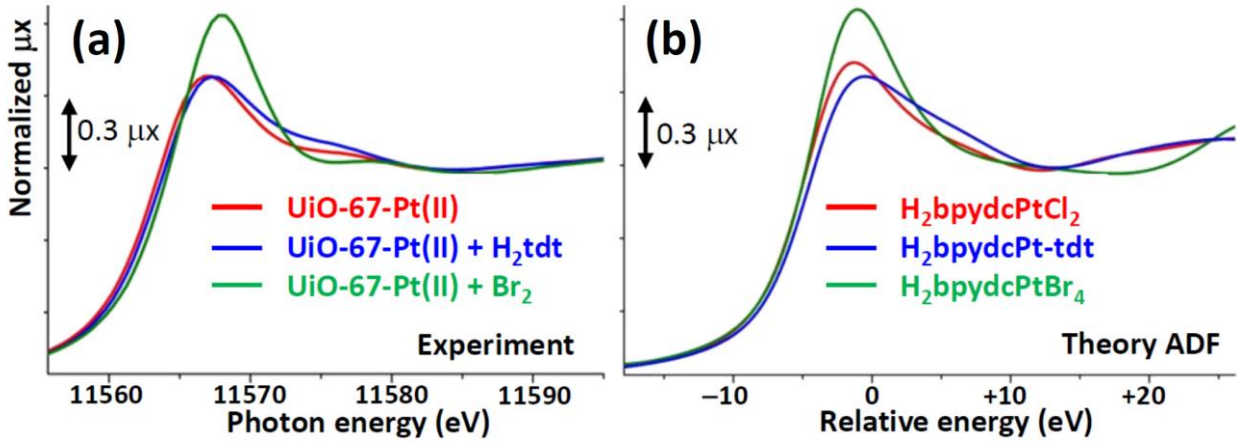

Figure 9. Part (a): experimental Pt L_3-edge XANES spectra of UiO-67-Pt(II) before (red line) and after interaction with H_2tdt (blue line) and Br_2 (green line). Part (b): As part (a) for the theoretical spectra computed with ADF code. Unpublished figure. Reproduced from Ref. [181].

3.3. Interaction of NH_3 with Cu^{2+} sites in HKUST-1

HKUST-1, also known as $Cu_3(BTC)_2$, is a Cu(II) based fcc-MOF characterized by a 3D system of square-shaped pores (9 Å × 9 Å).[182] In $Cu_3(BTC)_2$ Cu^{2+} ions form dimers, where each copper atom is coordinated to four oxygen atoms, coming from the benzene-1,3,5 tricarboxylate (BTC) linkers ($[Cu_2C_4O_8]$ cage) and one water molecule adsorbed on each Cu^{2+} site.[55,155,183] A schematic representation of the $Cu_3(BTC)_2$ buildings blocks and how they are connected to give rise to the three-dimensional structure is reported in Figure 10a. The EXAFS study of Prestipino et al.[155] showed that water molecules can be removed from the first coordination shell of Cu^{2+} without loss of crystallinity and porosity. This property is extremely important, as it implies the formation of coordinatively unsaturated Cu^{2+} sites that become consequently available for additional ligands such as molecules dosed from the gas phase (Figure 10b). EXAFS analysis revealed that water removal from the first coordination shell of Cu^{2+} causes an important modification of the $[Cu_2C_4O_8]$ cage resulting in a decrease of the Cu^{2+}-Cu^{2+} distance from (2.64 ± 0.02) Å down to (2.50 ± 0.02) Å.[155] Successively, Borfecchia et al.[158] repeated the experiment and confirmed the shrinking of the Cu^{2+}-Cu^{2+} distance upon dehydration previously observed by Prestipino et al., but to a smaller extent: from (2.65 ± 0.02) Å down to (2.58 ± 0.02) Å, see Table 2.

Borfecchia et al.[158] also investigated by EXAFS the coordination of NH_3 on the dehydrated material, observing that ammonia binds to Cu^{2+} at a distance of (2.31 ± 0.01) Å (while water coordinates at (2.24 ± 0.03) Å) and causes an impressive expansion of the Cu^{2+}-Cu^{2+} distance up to (2.80 ± 0.03) Å, see Table 2.

Of interest is also the XANES study reported by Borfecchia et al.[158] and here summarized in Figure 12. Part (a) reports the experimental XANES spectra of HKUST-1 as-prepared (hydrated sample, blue solid line), after activation at 453 K (dehydrated sample, pink solid line) and upon contact with 60 mbar of ammonia at room temperature (green solid line). The XANES spectra of the as prepared and dehydrated sample are typical of Cu(II) species, showing the edge jump at 8990 eV and two characteristic pre-edge peaks at ca. 8976 eV and ca. 8986 eV, labelled as **(1)** and **(2),** respectively, in Figure 12a, and separately reported in the insets of the same part. Feature **(1)** is assigned to the very weak $1s \rightarrow 3d$ quadupolar transition, while the shoulder **(2)** appearing along the white line profile is related to the dipolar shakedown $1s \rightarrow 4p$ transition.

Table 2. Summary of the Cu-Cu and Cu-L (L = H_2O or NH_3) bond distances in HKUST-1 MOF obtained by single crystal (SC) XRD and EXAFS. Previously unpublished table, reporting data published in the references quoted in the last column.

Ligand (L)	technique	Cu-Cu distance (Å)	Cu-L distance (Å)	Ref.
H_2O	SC XRD	2.628(2)	2.165(8)	[182]
H_2O	EXAFS	2.64(2)	2.19(2)	[155]
H_2O	EXAFS	2.65(2)	2.24(2)	[158]
–	EXAFS	2.50(2)	–	[155]
–	EXAFS	2.58(2)	–	[158]
NH_3	EXAFS	2.80(3)	2.31(1)	[158]

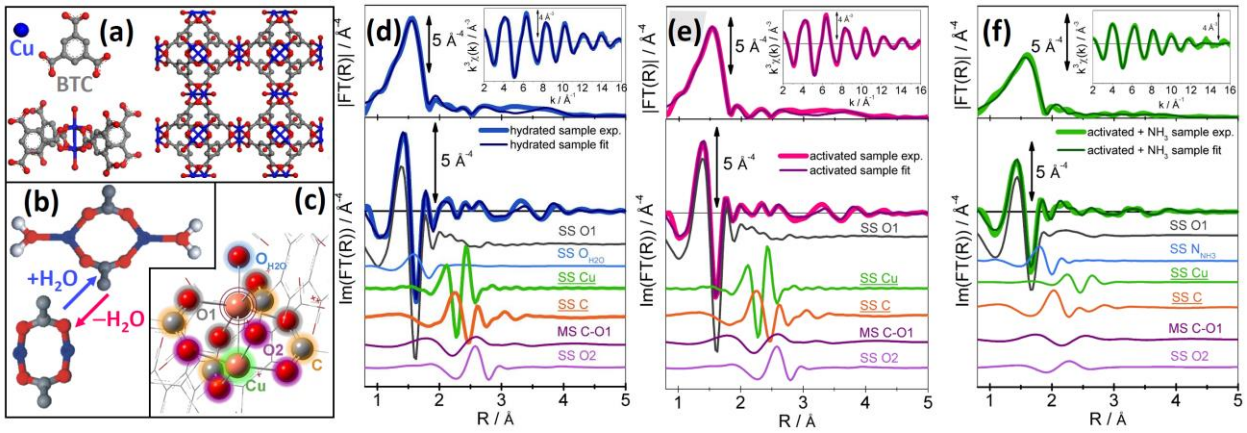

Figure 10. Part (a): Schematic representation of the building blocks of HKUST-1. Two Cu^{2+} ions, and four benzene-1,3,5 tricarboxilate (TMA) linkers are bounded to give rise the final 3D structure. The picture shows the typical paddle wheel coordination of Cu^{2+} sites. Water molecules directly bounded to Cu^{2+} are represented by an oxygen atom only. Part (b) top: hydrated $[Cu_2C_4O_8](H_2O)_2$ cluster. Part (b) bottom: dehydrated $[Cu_2C_4O_8]$ cage. Color code: Cu^{2+} (blue); O (red); C (grey) H (white). Part (c): cluster used as starting point for the fitting procedure of EXAFS data. Atoms color code is the following: Cu pale pink, C gray, O red. The groups of atoms involved in the principal paths contributing to EXAFS signal are labeled and highlighted by different colored halos (oxygen atoms of the TMA carboxyl groups directly coordinated to the Cu_{abs}, O1, gray; oxygen of the water molecule directly coordinated to the Cu absorber, O_{H2O}, light blue; second copper atom of the dimer in front of the absorber, Cu, green; the four carbon atoms of the TMA carboxyl groups, C, orange; oxygen atoms coordinated to the not absorber copper site, O2, purple). Parts (d), (e) and (f): Comparison between experimental and corresponding best fits for the hydrated (d), dehydrated (c) and dehydrated + NH_3 (d) sample. Top panels report the modulus of the FT, while bottom panels show the imaginary parts of the FT, and the principal paths contributions to the total signal. Parts (a,b) adapted with permission from Ref. [183], copyright RSC 2007; parts (c-f) adapted with permission from Ref. [158] copyright ACS (2012).

XANES spectra reported in Figure 12b were simulated using FEFF8.4 code.[133] For the hydrated version of HKUST-1 (blue spectrum) the authors adopted as input geometry the structure optimized in the single crystal XRD study of Chui et al.[182] and cutting a cluster centered on one of the Cu atoms with a radius of 6 Å around it. For a further improvement of the simulations, an optimization of geometrical parameters was performed exploiting FitIt software[184] and optimizing five structural parameters: (i) the Cu-Cu and (ii) Cu-H_2O bond length, the distance between the Cu atom and the TMA carboxyl groups with a separate optimization of (iii) Cu-O1 and of (iv) Cu-C and Cu-O2 distances (optimized in a correlated way to use only one free parameter) and (v) a general overall contraction or elongation of all the other distances ($R_{XANES} = \alpha\ R_{XRD}$).[126,185] See Figure 11c for the atom notation. It has been observed that a variation of Cu-Cu distance reflected in very slight changes in the XANES features, the Cu-H_2O distance influences the intensity and partially the position in energy of the pre-edge feature **(2)**, the carbonyl groups distances and a possible overall contraction or

expansion strongly influence both the intensity and the position of the white line and the shape of the multiple scattering features at higher energies.[158]

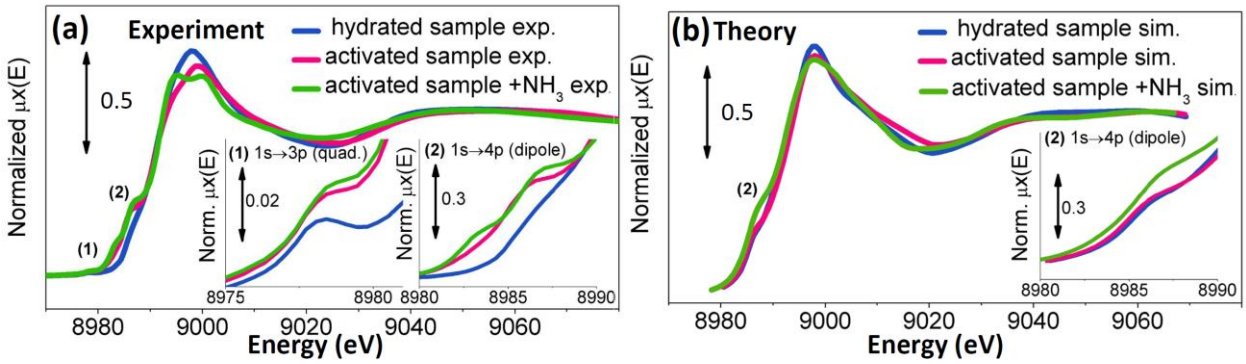

Figure 11. Part (a): Experimental XANES spectra of HKUST-1 in its hydrated (blue line) and dehydrated (pink line) forms and after successive interaction with NH_3 (green line). The insets report magnifications of the $1s \rightarrow 3d$ quadupolar transition **(1)** and of the shakedown 1s → 4p transition **(2)**. Part (b): as part (a) for the simulated spectra. Adapted with permission from Ref. [158] copyright ACS (2012).

The simulation of the dehydrated sample was obtained removing the water molecules from the previous cluster, while for the sample in interaction with ammonia the H_2O molecules were substituted by two NH_3 ones.[158] In the case of the hydrated sample, the best agreement between the simulated curve and experimental data was obtained with a slight shortening of Cu-H_2O distance, an elongation of 0.05 Å of both Cu-O1 and the constrained Cu-C and Cu-O2 distances, corresponding to a shift along the bond axis of the carbonyl groups and a slight general contraction of all other distances. Upon water removal, no shift in the absorption edge is observed, providing an evidence that no change in oxidation state of the Cu centre occurs. However, the XANES spectrum of the dehydrated sample shows: i) a decrease of the white line intensity, and ii) an increase in the intensity of feature **(2)**, that appears more as a well separated band than as a white line shoulder. The simulation of the XANES spectrum for the activated sample was performed with the same method previously described for the hydrated sample removing the atoms of the two water molecules, resulting in an optimization with four parameters only. Even without a structural optimization, in the simulated spectra it has been observed the same trend noticed on the experimental curves where the decrease of the white line intensity is correlated to the lower coordination number, and the increase of the intensity of feature **(2)** is ascribable to a lower symmetry of the Cu(II) species. The authors concluded that in the simulated curves this trend is less evident probably because a full description of the asymmetric distortion undergone by the Cu species in the activated sample would require a too high number of parameters to be optimized. The optimization of the bond distances resulted in a slight contraction of the distances between the absorbing Cu atom and carbonyl groups and all other distances, in agreement with the results found by EXAFS study (see Figure 11 and Table 2). The XANES spectrum of the activated sample after the interaction with NH_3 evidences an additional increase in the intensity and a slight blue-shift of the dipole band **(2)** assigned to the 1s → 4p transition.[158] Moreover, a new pre-edge peak is observed at ca. 8983 eV. Despite the edge position is not modified respect to the as prepared and activated samples (no change in oxidation state of the metal), the white line is modified towards a more structured appearance, and seems to return towards the shape observed in the case of the hydrated sample. The simulation of the spectrum for the sample after interaction with NH_3 was performed following the same method adopted for the hydrated material and substituting the water molecules with two NH_3 molecules. After the optimization of the geometrical parameters it has been observed that an increasing of the intensity of the pre-edge feature **(2)** is

proportional to the Cu-NH_3 distance which was optimized at 2.3 Å with a considerable elongation with respect to the previous position of the water molecules. Moreover a splitting of the white line feature, even if less evident with respect to the experimental spectra, has been observed after a distortion of carbonyl groups simulated by a slight elongation of Cu-O1 distances but a severe shortening of both Cu-C and Cu-O2 and all other distances. The authors concluded that that the deformation introduced to simulate the XANES spectra is in agreement with the results of the EXAFS fit.[158]

3.4. Discrimination between phosphine and phosphine oxide groups in P-MOFs by P K-edge XAS

Phosphine metal–organic frameworks (P-MOFs) are crystalline porous coordination polymers that contain phosphorus functional groups within their pores.[186-191] Incorporation of phosphine functional groups inside structures with new and existing topologies is achieved using direct solvothermal synthesis, postsynthetic modification[192] or the co-crystallization of organic linkers with similar connectivity.[193] Interesting applications for this new class of materials have been foreseen in transition metal immobilization and catalysis.[187,194]

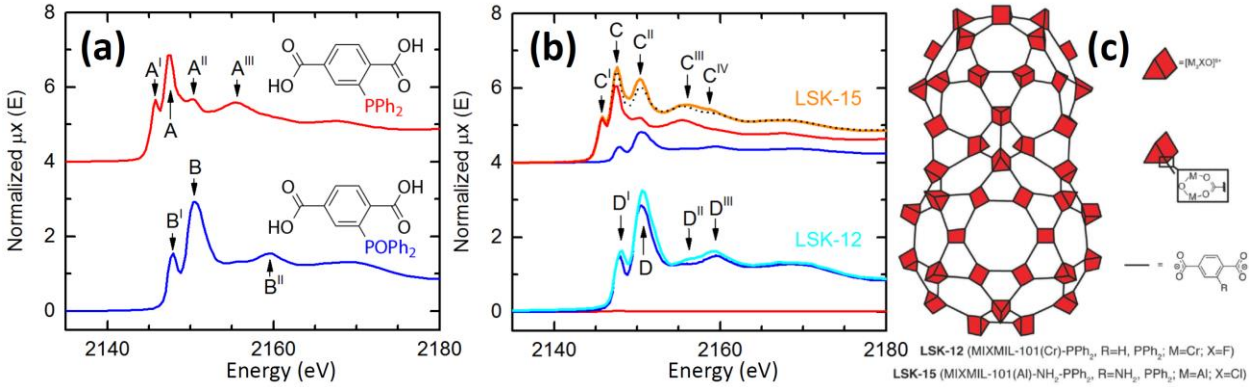

Figure 12. Part (a): P K-edge XANES spectra of the PPh_2-BDC (red curve) and $POPh_2$-BDC (blue curve) organic linkers. Also reported are the linker structure and the peak labeling. Part (b): P K-edge XANES spectra of LSK-15 (orange curve) and LSK-12 (cyan curve) P-MOFs with MIL-101 topology. The red and blue spectra represent the weighted fraction of the linker spectra, see part (a), used to reproduce the XANES spectra of the P-MOFs with a linear combination approach (dotted spectrum). Part (c): Schematic representation of P-MOFs with MIL-101 topology. Adapted with permission from Ref. [191], copyright Royal Society of Chemistry (2015).

Very recently Morel et al.[191] used soft-X-ray P-K-edge XAS to determine the phosphine to phosphine oxide ratio in two P-MOFs with MIL-101 topology, shich structure is described in Figure 12c. This achievement is of particular relevance as e phosphorus oxidation state is of particular interest as the phosphine to phosphine oxide ratio influences the coordination affinity of P-MOFs for transition metals. Differently to solid state NMR spectroscopy, P-K-edge XAS can determine the oxidation state of phosphorus even when the material contains paramagnetic nuclei.

The P K-edge XAS spectra of PPh_2-BDC and $POPh_2$-BDC linkers, see Figure 12a red and blue spectra respectively, provide a spectral reference for the characterization of the two P-MOFs. A blue shift in the white line from 2147.3 to 2150.6 eV is observed upon oxidation of the phosphorus nuclei, compare the pre-edge resonances (A^I and B^I in Figure 12a), that are attributed to the effect of phenyl groups in the higher coordination shells of the phosphorus.[195] The spectrum of PPh_2-BDC exhibits a more pronounced pre-edge feature relative to its white line, compared to that of the $POPh_2$-BDC linker. Spectral features are not affected equally by the presence of an oxygen atom, with a 2.2 eV shift for A^I to B^I features compared to a 3.3 eV for the A to B white lines. PPh_2-BDC displayed an additional spectral feature A^{II} at an energy very close

to that of the white line of $POPh_2$-BDC (2150.3 eV) and indicates partial oxidation of the sample in agreement with a parallel ^{31}P NMR investigation.[191]

The P K-edge XANES spectra of LSK-15 and LSK-12 P-MOFs are reported in Figure 12b, orange and cyan spectra, respectively. The former P-MOF is characterized by a complex XANES spectrum defined by five different absorption features (C to C^{IV}), which testifies the presence of multiple phosphorus oxidation states. As for PPh_2-BDC linker, LSK-15 displayed features related to the white lines of triarylphosphine (C) and triarylphosphine oxide (C^{II}) at 2145.7 and 2150.2 eV, respectively. The relative intensity of C^{II} to C ratio is higher in LSK-15 than in the corresponding A^{II} to A ratio in the organic linker PPh_2-BDC providing proof of phosphorus oxidation inside this MOF. The pre-edge feature C^{I} is attributed to the characteristic resonance of phosphine environment in PPh_2-BDC. The XANES spectrum of LSK-12 displays fewer features than LSK-15 (D to D^{III}). Comparison based solely on the absorption edge positions of the two organic linkers is difficult due to a perceived overlap between A and B^{I}, which could both be contributors to the D^{I} feature. However, the absence of the corresponding A^{I} preedge feature in LSK-12, and to a lesser extent the small edge shift between C and D^{I}, are indicative of phosphine oxide as the primary phosphorus species in LSK-12. The relative intensities of the white line D and the pre-edge feature D^{I} also compare well with the $POPh_2$-BDC organic linker. Finally, Morel et al.,[191] reproducing the XANES spectrum of the P-MOF samples with a linear combination of the spectra of the linkers concluded that phosphine accounts for about 70 % of the total phosphorus groups in LSK-15 and that LSK-12 contains only phosphine oxide, see Figure 12b.

3.5. Optimized finite difference method for the full-potential XANES simulations: application to molecular adsorption geometries in MOFs

Over the past two decades much progress has been made in the understanding the features of the XANES region of the X-ray absorption spectra.[133,134,137,140,196-205]

As already outlined at the end of section 3.3 (see Figure 11 and related discussion) appearance of progressively more sophisticated codes, together with the increased computational capabilities, has made XANES a spectroscopy able to quantitatively confirm or discard a structural model for the environment of the X-ray absorbing atom, forming thus a new fundamental diagnostic tool in condensed matter physics and chemistry.[119,148,149,206] Besides the multiple scattering approach (used e.g. by, FEFF,[133] XKDQ,[207] CONTINUUM,[208,209] MXAN.[138,139] etc… codes) the Finite Difference Method (FDM)[140,205] is attractive for calculations of the photoelectron wave function up to 100−200 eV above the absorption edge avoiding, in a simple way, the muffin tin approximation used in the multiple scattering theory approaches. In the muffin tin approximation, the potential is assumed to be spherical inside the touching (or overlapping) atomic spheres and constant between them.[134] The main drawback of the XANES simulation in the FDM approach is the heavy computational time and the huge RAM required to store the computed values. Very recently, due to the use of dedicated solvers for sparse matrices, Guda et al.[141] succeeded in reducing by more than one order of magnitude the required CPU time and in halving the needed RAM required by the standard Gaussian method previously used by the FDMNES code.[140] The potentialities of this improved version of the FDMNES code are hereafter discussed using as example the Ni K-edge XANES spectra of CPO-27-Ni MOF and its modification upon molecular adsorption on the Ni site.

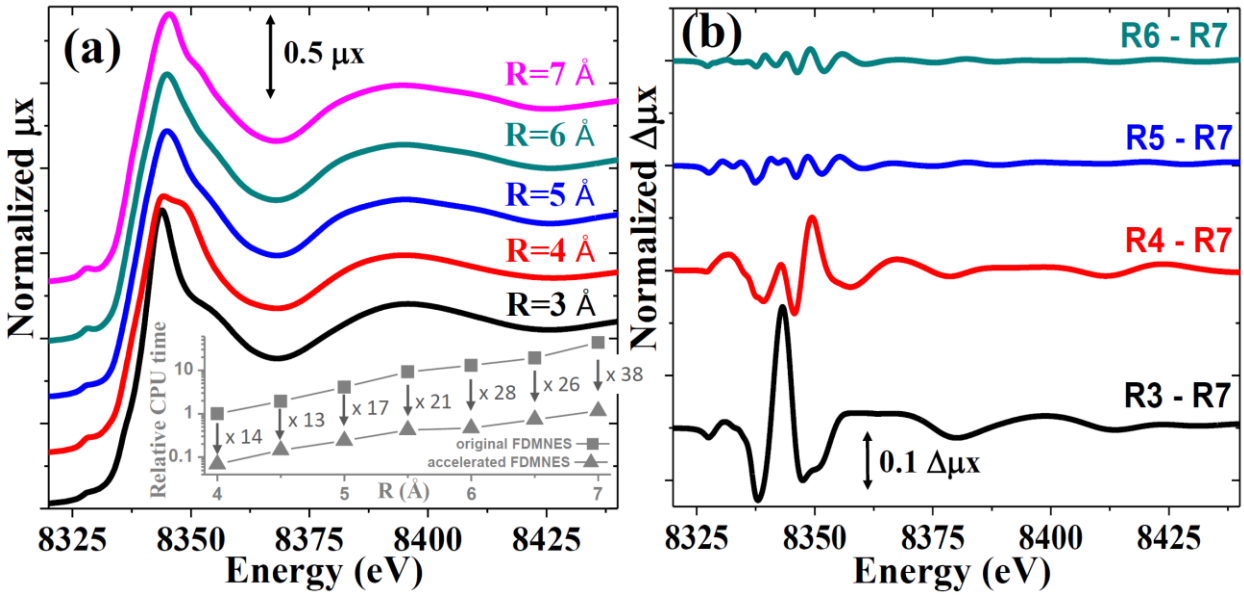

Figure 13. Part (a): normalized theoretical Ni K-edge XANES spectra computed with the FDNMES code as a function of cluster size used in calculations for the CPO-27-Ni structure. The inset reports, in logarithmic scale, the relative CPU time needed to run the XANES simulation on the cluster of radius R with the original FDMNES code (squares) and with the new accelerated version (triangles), with respect to the time needed for the R = 4 Å simulation with the original version of the code. The numbers close to the vertical arrows represent the speed-up factor for a given cluster size defined as CPU(original)/CPU(accelerated). Part (b): difference XANES spectra calculated for the spectra reported in part (a) with respect to R = 7 Å simulation. In both panels the spectra are shifted vertically for the sake of clarity. For a view of the CPO-27-Ni structure, see Figure 3. Adapted with permission from Ref. [141], copyright American Chemical Society (2015).

CPO-27-Ni MOF[122] contains one-dimensional channels which are filled with water that can be removed by a mild thermal treatment. Upon dehydration the crystalline structure is preserved and a material with a high surface area containing unsaturated metal sites organized in helicoidal chains is obtained,[126] see above Figure 3d. In its dehydrated form the first coordination of Ni^{2+} atoms consists into five framework oxygen atoms in a square planar pyramidal-like configuration, leaving one coordination vacancy free for adsorbate coordination adsorbate molecules such as: CO,[125] H_2O,[126] NO,[126] N_2,[123] C_2H_4,[123] H_2S.[210] As shown above in Figure 3c, the adsorption of a molecule into the coordination vacancy of Ni^{2+} causes week, but significant, changes in the Ni K-edge XANES spectrum of CPO-27-Ni. As just outlined, the XANES simulation in the FDM approach is CPU time consuming. Indeed, a large cluster must be cut around the Ni atom that undergoes the photoelectric effect before reaching convergence of the XANES calculations. This fact is clearly shown in Figure 13a showing that the simulated XANES spectrum of the dehydrated form of CPO-27-Ni changes significantly moving from a cluster cut R = 3 Å to one cut at R = 5 Å. This fact is even more evident in Figure 13b where the difference spectra are shown: $\Delta\mu_{7,R}^{theo}(E) = \mu_7^{theo}(E) - \mu_R^{theo}(E)$. Unfortunately, the CPU needed to perform the XANES simulation scales approximatively with an exponential function of the cluster size, as shown by the scattered squares reported in the inset of Figure 13a, that are almost linear in a logarithmic ordinate scale. This means that the simulation on the R = 7 Å cluster is 44 times more demanding than that on the R = 4 cluster; moreover it requires 14 times more RAM memory (data not reported in the inset). The accelerated version of the FDMNES code,[141] reduces significantly the requested CPU time for the same calculations, see scattered triangles in the inset of Figure 13a. Of particular interest is the fact that the speed-up of the calculations (defined as the ratio between the CPU time needed in to perform a given calculation in the standard code divided by the time needed for the same calculation with the

accelerated version of the code) scales favorably with the increasing cluster size: with some fluctuations it moves from 14 to 38 moving from the R = 4 Å cluster to the R = 7 Å one (see the numbers reported close to the vertical arrows in the inset).

The gain of a factor larger than one order of magnitude (up to forty for the large clusters relevant to obtain a meaningful simulation) makes it possible to perform structural determination from a detailed XANES study. To prove this concept we will show that it is possible form the simulation of the XANES spectra to determine the geometry of the molecular complex formed upon adsorption of a diatomic ligand molecule (NO or CO) on the coordination vacancy of Ni^{2+} sites in the dehydrated form of CPO-27-Ni MOF. As the spectroscopic difference between the XANES spectra collected before and after molecular adsorption are not very large (see e.g. the case of N_2 adsorption reported in Figure 3c), they are better appreciated by reporting the difference spectra $\Delta\mu^{exp} = \mu^{exp}(+NO) - \mu^{exp}(dehyd)$, as done in the scattered dots spectrum reported in Figure 14a, for the case of NO adsorption. Also reported (red curve) is the analogous difference spectrum obtained from the simulations: $\Delta\mu^{theo,\theta} = \mu^{theo,\theta}(+NO) - \mu^{theo}(dehyd)$. As shown in Figure 14b, $\mu^{theo,\theta}(+NO)$, an thus $\Delta\mu^{theo,\theta}(+NO)$, depends on the adsorption geometry of the NO molecule, in particular on the adsorption angle Ni-N-O (θ).

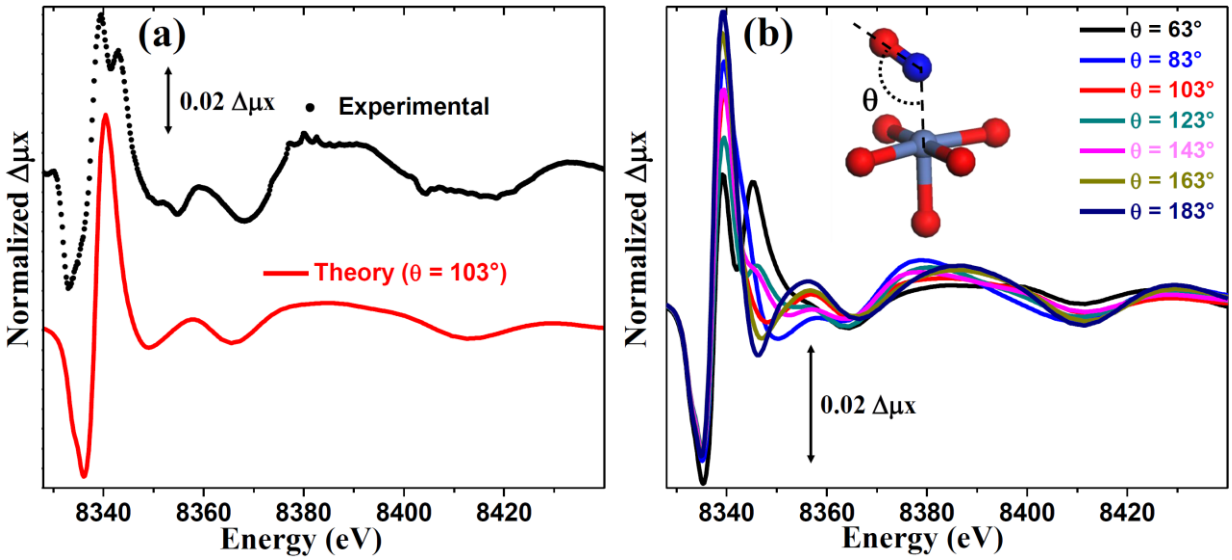

Figure 14. Part (a): Difference XANES spectrum obtained subtracting the spectrum of the dehydrated CPO-27-Ni MOF form that obtained after dosing NO on the same sample (black scattered dots). The red spectrum is the analogous difference XANES spectrum obtained from the subtracting the spectra obtained with the FDMNES simulations with a Ni-N-O angle (θ) of 103°. Part (b): Effect of θ in the computed difference XANES spectra. The inset reports, with the sticks and balls drawing, a cartoon of the first shell around Ni (lilac) formed by five framework O (red) plus the coordinated NO molecule, N (blue), defining the θ angle. Previously unpublished figure reporting data discussed in Ref. [141].

The simulations reported in Figure 14b clearly indicate that it is possible to determine the adsorption angle θ by an appropriate comparison between the experimental Δμ and the theoretical ones computed for different θ angles. The red squares in Figure 15 reports the integrated difference over all the sampled points of $|\Delta\mu^{exp}(E_i) - \Delta\mu^{theo,\theta}(E_i)|$ in the 8325-8440 eV interval plotted versus the adsorption angle θ used in the simulations. From the results it is evident that the linear geometry is not favored and that the XANES simulations predict a bent geometry for the Ni···NO adducts with a θ angle in the 90-140 ° range. Conversely, for the CO adsorption (scattered black circles in Figure 15) the linear geometry (θ ~ 180°) is clearly favored. These results are in agreement with the periodic DFT calculation performed by

Valenzano et al.[124] where the optimized structures were characterized by adsorption angles of Ni–N–O = 123° and of Ni–C–O = 171°, while the fitting of the EXAFS data resulted in good agreement with the experimental data by fixing the adsorption angles to Ni–N–O = 130° and of Ni–C–O = 180°.[125,126]

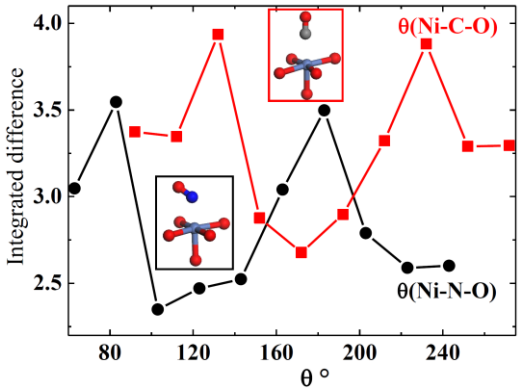

Figure 15. Integrated difference over all the sampled points of $|\Delta\mu^{exp}(E_i) - \Delta\mu^{theo,\theta}(E_i)|$ in the 8325-8440 eV interval plotted versus the adsorption angle θ used in the simulations. Red squares and black circles refer to the CO and NO adsorption, respectively. The inset reports, with the sticks and balls drawing, a cartoon of the first shell around Ni of the carbonyl and nitisol adducts formed inside CPO-27-Ni MOF: Ni(lilac), O (red), N (blue), C (grey). Adapted with permission from Ref. [141], copyright American Chemical Society (2015).

6. Conclusions

In this chapter, we have introduced MOFs as the new class of crystalline porous materials of remarkable potentialities. We have underlined the flexibility in the realization of different MOFs frameworks and the fact that they are ideal materials for performing X-ray absorption experiments at the metal K or L_{III} edges in transmission mode. A selection of relevant results appearing in the last five years follows, underlying the relevant role of both EXAFS and XANES in determining the structural and electronic configuration of metals centers inside MOFs frameworks.

Acknowledgements

We acknowledge C. Prestipino, D. Gianolio G. Agostini, S. Jakobsen, M.H. Nilsen, P.D.C. Dietzel, A. A. Guda, A. L. Bugaev, A. V. Soldatov and F. Morel for the their contribution to some of the results here reviewed. We are indebted to F. Morel for having kindly provided a new color version of Figure 12. KAL, AAG, MAS and CL acknowledge the Mega-grant of the Russian Federation Government to support scientific research at the Southern Federal University, No. 14.Y26.31.0001.

References

1. Cheetham AK, Ferey G, Loiseau T (1999) Open-framework inorganic materials. Angew. Chem.-Int. Edit., 38: 3268-3292.
2. James SL (2003) Metal-organic frameworks. Chem. Soc. Rev., 32: 276-288.
3. Bradshaw D, Claridge JB, Cussen EJ et al (2005) Design, chirality, and flexibility in nanoporous molecule-based materials. Accounts Chem. Res., 38: 273-282.
4. Ferey G (2008) Hybrid porous solids: past, present, future. Chem. Soc. Rev., 37: 191-214.
5. O'Keeffe M (2009) Design of MOF and intellectual content in reticular chemistry: a personal view. Chem. Soc. Rev., 38: 1215-1217.
6. Perry IV JJ, Perman JA, Zaworotko MJ (2009) Design and synthesis of metal-organic frameworks using metal-organic polyhedra as supramolecular building blocks. Chem. Soc. Rev., 38: 1400-1417.
7. Morris RE, Bu XH (2010) Induction of chiral porous solids containing only achiral building blocks. Nat. Chem., 2: 353-361.
8. Furukawa H, Ko N, Go YB et al (2010) Ultrahigh Porosity in Metal-Organic Frameworks. Science, 329: 424-428.

9. Farha OK, Hupp JT (2010) Rational Design, Synthesis, Purification, and Activation of Metal-Organic Framework Materials. Accounts Chem. Res., 43: 1166-1175.
10. Seeber G, Cooper GJT, Newton GN et al (2010) Following the self assembly of supramolecular MOFs using X-ray crystallography and cryospray mass spectrometry. Chem. Sci., 1: 62-67.
11. Bordiga S, Bonino F, Lillerud KP et al (2010) X-ray absorption spectroscopies: useful tools to understand metallorganic frameworks structure and reactivity. Chem. Soc. Rev., 39: 4885-4927.
12. Zhou HC, Long JR, Yaghi OM (2012) Introduction to Metal-Organic Frameworks. Chem. Rev., 112: 673-674.
13. Furukawa H, Cordova KE, O'Keeffe M et al (2013) The Chemistry and Applications of Metal-Organic Frameworks. Science, 341: 1230444-1230444.
14. Llabrés i Xamena F, Gascon J, *Metal Organic Frameworks as Heterogeneous Catalysts*, The Royal Society of Chemistry, Cambridge, 2013.
15. Colon YJ, Snurr RQ (2014) High-throughput computational screening of metal-organic frameworks. Chem. Soc. Rev., 43: 5735-5749.
16. Schneemann A, Bon V, Schwedler I et al (2014) Flexible metal-organic frameworks. Chem. Soc. Rev., 43: 6062-6096.
17. Zhu QL, Xu Q (2014) Metal-organic framework composites. Chem. Soc. Rev., 43: 5468-5512.
18. Butova VV, Soldatov MA, A. GA et al (2015) Metal-Organic Frameworks: Structure, Properties, Synthesis, and Characterization. Russ. Chem. Rev., 84: DOI:10.1070/RCR4554
19. Ferey G (2001) Microporous solids: From organically templated inorganic skeletons to hybrid frameworks ... ecumenism in chemistry. Chem. Mater., 13: 3084-3098.
20. Eddaoudi M, Moler DB, Li HL et al (2001) Modular chemistry: Secondary building units as a basis for the design of highly porous and robust metal-organic carboxylate frameworks. Accounts Chem. Res., 34: 319-330.
21. Long JR, Yaghi OM (2009) The pervasive chemistry of metal-organic frameworks. Chem. Soc. Rev., 38: 1213-1214.
22. Baerlocher C, Meier WM, Olson DH, *Atlas of Zeolite Frameworks Types*, Elsevier, Amsterdam, 2001.
23. Tranchemontagne DJ, Mendoza-Cortes JL, O'Keeffe M et al (2009) Secondary building units, nets and bonding in the chemistry of metal-organic frameworks. Chem. Soc. Rev., 38: 1257-1283.
24. Eddaoudi M, Kim J, Rosi N et al (2002) Systematic Design of Pore Size and Functionality in Isoreticular MOFs and Their Application in Methane Storage. Science, 295: 469-472.
25. Cavka JH, Jakobsen S, Olsbye U et al (2008) A new zirconium inorganic building brick forming metal organic frameworks with exceptional stability. J. Am. Chem. Soc., 130: 13850-13851.
26. Valenzano L, Civalleri B, Bordiga S et al (2011) Disclosing the complex structure of UiO-66 MOF: a synergic combination of experiment and theory. Chem. Mater., 23: 1700-1718.
27. Chavan S, Vitillo JG, Gianolio D et al (2012) H_2 storage in isostructural UiO-67 and UiO-66 MOFs. Phys. Chem. Chem. Phys., 14: 1614-1626.
28. Lillerud K, Olsbye U, Tilset M (2010) Designing Heterogeneous Catalysts by Incorporating Enzyme-Like Functionalities into MOFs. Top Catal, 53: 859-868.
29. Müller U, Schubert M, Teich F et al (2006) Metal-organic frameworks - prospective industrial applications. J. Mater. Chem., 16: 626-636.
30. Czaja A, Trukhan T, Müller U (2009) Industrial applications of metal-organic frameworks. Chem. Soc. Rev., 38: 1284-1293.
31. Li J-R, Luppler RJ, Zhou HC (2009) Selective gas adsorption and separation in metal-organic frameworks. Chem. Soc. Rev., 38: 1477-1504.
32. Shimomura S, Higuchi M, Matsuda R et al (2010) Selective sorption of oxygen and nitric oxide by an electron-donating flexible porous coordination polymer. Nat. Chem., 2: 633-637.
33. Li JR, Sculley J, Zhou HC (2012) Metal-Organic Frameworks for Separations. Chem. Rev., 112: 869-932.
34. Qiu SL, Xue M, Zhu GS (2014) Metal-organic framework membranes: from synthesis to separation application. Chem. Soc. Rev., 43: 6116-6140.
35. Dinca M, Long JR (2005) Strong H_2 binding and selective gas adsorption within the microporous coordination solid $Mg_3(O_2C\text{-}C_{10}H_6\text{-}CO_2)_3$. J. Am. Chem. Soc., 127: 9376-9377.
36. Vitillo JG, Savonnet M, Ricchiardi G et al (2011) Tailoring Metal-Organic Frameworks for CO_2 Capture: The Amino Effect. ChemSusChem, 4: 1281-1290.
37. Chaemchuen S, Kabir NA, Zhou K et al (2013) Metal-organic frameworks for upgrading biogas via CO_2 adsorption to biogas green energy. Chem. Soc. Rev., 42: 9304-9332.
38. Cabello CP, Berlier G, Magnacca G et al (2015) Enhanced CO_2 adsorption capacity of amine-functionalized MIL-100(Cr) metal-organic frameworks. CrystEngComm, 430-437.
39. Rodenas T, Luz I, Prieto G et al (2015) Metal–organic framework nanosheets in polymer composite materials for gas separation. Nat. Mater., 14: 48-55.
40. Ferey G, Serre C, Devic T et al (2011) Why hybrid porous solids capture greenhouse gases? Chem. Soc. Rev., 40: 550-562.

41. Sumida K, Rogow DL, Mason JA et al (2012) Carbon Dioxide Capture in Metal-Organic Frameworks. Chem. Rev., 112: 724-781.
42. McDonald TM, Mason JA, Kong XQ et al (2015) Cooperative insertion of CO_2 in diamine-appended metal-organic frameworks. Nature, 519: 303-308.
43. Matsuda R, Tsujino T, Sato H et al (2010) Temperature responsive channel uniformity impacts on highly guest-selective adsorption in a porous coordination polymer. Chem. Sci., 1: 315-321.
44. Pan L, Olson DH, Ciemnolonski LR et al (2006) Separation of hydrocarbons with a microporous metal-organic framework. Angew. Chem.-Int. Edit., 45: 616-619.
45. Barea E, Montoro C, Navarro JAR (2014) Toxic gas removal - metal-organic frameworks for the capture and degradation of toxic gases and vapours. Chem. Soc. Rev., 43: 5419-5430.
46. DeCoste JB, Peterson GW (2014) Metal-Organic Frameworks for Air Purification of Toxic Chemicals. Chem. Rev., 114: 5695-5727.
47. Suh K, Yutkin MP, Dybtsev DN et al (2012) Enantioselective sorption of alcohols in a homochiral metal-organic framework. Chem. Commun., 48: 513-515.
48. Van de Voorde B, Bueken B, Denayer J et al (2014) Adsorptive separation on metal-organic frameworks in the liquid phase. Chem. Soc. Rev., 43: 5766-5788.
49. Getman RB, Bae YS, Wilmer CE et al (2012) Review and Analysis of Molecular Simulations of Methane, Hydrogen, and Acetylene Storage in Metal-Organic Frameworks. Chem. Rev., 112: 703-723.
50. Wu HH, Gong QH, Olson DH et al (2012) Commensurate Adsorption of Hydrocarbons and Alcohols in Microporous Metal Organic Frameworks. Chem. Rev., 112: 836-868.
51. Vitillo JG, Regli L, Chavan S et al (2008) Role of exposed metal sites in the hydrogen storage in MOFs. J. Am. Chem. Soc., 130: 8386-8396.
52. Murray LJ, Dinca M, Long JR (2009) Hydrogen storage in metal-organic frameworks. Chem. Soc. Rev., 38: 1294-1314.
53. Han SS, Mendoza-Cortes JL, Goddard WA (2009) Recent advances on simulation and theory of hydrogen storage in metal-organic frameworks and covalent organic frameworks. Chem. Soc. Rev., 38: 1460-1476.
54. Rossin A, Di Credico B, Giambastiani G et al (2012) Synthesis, characterization and CO_2 uptake of a chiral Co(II) metal-organic framework containing a thiazolidine-based spacer. J. Mater. Chem., 22: 10335-10344.
55. Xiao B, Wheatley PS, Zhao XB et al (2007) High-capacity hydrogen and nitric oxide adsorption and storage in a metal-organic framework. J. Am. Chem. Soc., 129: 1203-1209.
56. Horcajada P, Chalati T, Serre C et al (2010) Porous metal-organic-framework nanoscale carriers as a potential platform for drug delivery and imaging. Nat. Mater., 9: 172-178.
57. Horcajada P, Gref R, Baati T et al (2012) Metal-Organic Frameworks in Biomedicine. Chem. Rev., 112: 1232-1268.
58. Bloch ED, Queen WL, Chavan S et al (2015) Gradual Release of Strongly Bound Nitric Oxide from $Fe_2(NO)_2$(dobdc). J. Am. Chem. Soc., 137: 3466-3469.
59. Bunzli JCG, Piguet C (2002) Lanthanide-containing molecular and supramolecular polymetallic functional assemblies. Chem. Rev., 102: 1897-1928.
60. Bordiga S, Lamberti C, Ricchiardi G et al (2004) Electronic and vibrational properties of a MOF-5 metal-organic framework: ZnO quantum dot behaviour. Chem. Commun., 2300-2301.
61. Allendorf MD, Bauer CA, Bhakta RK et al (2009) Luminescent metal-organic frameworks. Chem. Soc. Rev., 38: 1330-1352.
62. Kovalenko KA, Dybtsev DN, Lebedkin SF et al (2010) Luminescence properties of mesoporous chromium(III) terephthalate and inclusion compounds of cluster complexes. Russ. Chem. Bull., 59: 741-744.
63. Wang C, Zhang T, Lin WB (2012) Rational Synthesis of Noncentrosymmetric Metal-Organic Frameworks for Second-Order Nonlinear Optics. Chem. Rev., 112: 1084-1104.
64. Cui YJ, Yue YF, Qian GD et al (2012) Luminescent Functional Metal-Organic Frameworks. Chem. Rev., 112: 1126-1162.
65. Heine J, Muller-Buschbaum K (2013) Engineering metal-based luminescence in coordination polymers and metal-organic frameworks. Chem. Soc. Rev., 42: 9232-9242.
66. Cui YJ, Chen BL, Qian GD (2014) Lanthanide metal-organic frameworks for luminescent sensing and light-emitting applications. Coord. Chem. Rev., 273: 76-86.
67. Hu ZC, Deibert BJ, Li J (2014) Luminescent metal-organic frameworks for chemical sensing and explosive detection. Chem. Soc. Rev., 43: 5815-5840.
68. Sato H, Matsuda R, Sugimoto K et al (2010) Photoactivation of a nanoporous crystal for on-demand guest trapping and conversion. Nat. Mater., 9: 661-666.
69. Kurmoo M (2009) Magnetic metal-organic frameworks. Chem. Soc. Rev., 38: 1353-1379.
70. Zhang W, Xiong RG (2012) Ferroelectric Metal-Organic Frameworks. Chem. Rev., 112: 1163-1195.
71. Horike S, Umeyama D, Kitagawa S (2013) Ion Conductivity and Transport by Porous Coordination Polymers and Metal-Organic Frameworks. Accounts Chem. Res., 46: 2376-2384.

72. Yamada T, Otsubo K, Makiura R et al (2013) Designer coordination polymers: dimensional crossover architectures and proton conduction. Chem. Soc. Rev., 42: 6655-6669.
73. Canivet J, Fateeva A, Guo YM et al (2014) Water adsorption in MOFs: fundamentals and applications. Chem. Soc. Rev., 43: 5594-5617.
74. Stavila V, Talin AA, Allendorf MD (2014) MOF-based electronic and optoelectronic devices. Chem. Soc. Rev., 43: 5994-6010.
75. Lee J, Farha OK, Roberts J et al (2009) Metal-organic framework materials as catalysts. Chem. Soc. Rev., 38: 1450-1459.
76. Corma A, Garcıa H, Llabres i Xamena FX (2010) Engineering Metal Organic Frameworks for Heterogeneous Catalysis. Chem. Rev., 110: 4606-4655.
77. Ranocchiari M, van Bokhoven JA (2011) Catalysis by metal-organic frameworks: fundamentals and opportunities. Phys. Chem. Chem. Phys., 13: 6388-6396.
78. Llabres i Xamena FX, Gascon J (2013) Towards Future MOF Catalytic Applications. In F. Llabrés i Xamena and J. Gascon (eds), Metal Organic Frameworks as Heterogeneous Catalysts, The Royal Society of Chemistry, Cambridge, pp. 406-424.
79. Vermoortele F, Valvekens P, De Vos D (2013) Catalysis at the Metallic Nodes of MOFs. In F. Llabrés i Xamena and J. Gascon (eds), Metal Organic Frameworks as Heterogeneous Catalysts, The Royal Society of Chemistry, pp. 268-288.
80. Kesanli B, Lin WB (2003) Chiral porous coordination networks: rational design and applications in enantioselective processes. Coord. Chem. Rev. , 246: 305-326.
81. Ma L, Abney C, Lin W (2009) Enantioselective catalysis with homochiral metal-organic frameworks. Chem. Soc. Rev., 38: 1248-1256.
82. Yoon M, Srirambalaji R, Kim K (2012) Homochiral Metal-Organic Frameworks for Asymmetric Heterogeneous Catalysis. Chem. Rev., 112: 1196-1231.
83. Falkowski JM, Liu S, Lin W (2013) Asymmetric Catalysis with Chiral Metal Organic Frameworks. In F. Llabrés i Xamena and J. Gascon (eds), Metal Organic Frameworks as Heterogeneous Catalysts, The Royal Society of Chemistry, Cambridge, pp. 344-364.
84. Leus K, Liu YY, Van Der Voort P (2014) Metal-Organic Frameworks as Selective or Chiral Oxidation Catalysts. Catal. Rev.-Sci. Eng., 56: 1-56.
85. Silva CG, Luz I, Llabres i Xamena FX et al (2010) Water Stable Zr-Benzenedicarboxylate Metal-Organic Frameworks as Photocatalysts for Hydrogen Generation. Chem.-Eur. J., 16: 11133-11138.
86. Garcia H, Ferrer B (2013) Photocatalysis by MOFs. In F. Llabrés i Xamena and J. Gascon (eds), Metal Organic Frameworks as Heterogeneous Catalysts, The Royal Society of Chemistry, Cambridge, pp. 365-383.
87. Qiu SL, Zhu GS (2009) Molecular engineering for synthesizing novel structures of metal-organic frameworks with multifunctional properties. Coord. Chem. Rev., 253: 2891-2911.
88. Wang Z, Cohen SM (2009) Postsynthetic modification of metal-organic-frameworks. Chem. Soc. Rev., 38: 1315-1329.
89. Deng HX, Doonan CJ, Furukawa H et al (2010) Multiple Functional Groups of Varying Ratios in Metal-Organic Frameworks. Science, 327: 846-850.
90. Chen BL, Xiang SC, Qian GD (2010) Metal-Organic Frameworks with Functional Pores for Recognition of Small Molecules. Accounts Chem. Res., 43: 1115-1124.
91. Tanabe KK, Cohen SM (2011) Postsynthetic modification of metal-organic frameworks-a progress report. Chem. Soc. Rev., 40: 498-519.
92. Cohen SM (2012) Postsynthetic Methods for the Functionalization of Metal-Organic Frameworks. Chem. Rev., 112: 970-1000.
93. Llabres i Xamena FX, Luz I, Cirujano FG (2013) Strategies for Creating Active Sites in MOFs. In F. Llabrés i Xamena and J. Gascon (eds), Metal Organic Frameworks as Heterogeneous Catalysts, The Royal Society of Chemistry, pp. 237-267.
94. Mondloch JE, Farha OK, Hupp JT (2013) Catalysis at the Organic Ligands. In F. Llabrés i Xamena and J. Gascon (eds), Metal Organic Frameworks as Heterogeneous Catalysts, The Royal Society of Chemistry, Cambridge, pp. 289-309.
95. Burrows AD (2013) Post-synthetic Modification of MOFs. In F. Llabrés i Xamena and J. Gascon (eds), Metal Organic Frameworks as Heterogeneous Catalysts, The Royal Society of Chemistry, Cambridge, pp. 31-75.
96. Deria P, Mondloch JE, Karagiaridi O et al (2014) Beyond post-synthesis modification: evolution of metal-organic frameworks via building block replacement. Chem. Soc. Rev., 43: 5896-5912.
97. Evans JD, Sumby CJ, Doonan CJ (2014) Post-synthetic metalation of metal-organic frameworks. Chem. Soc. Rev., 43: 5933-5951.
98. Lu WG, Wei ZW, Gu ZY et al (2014) Tuning the structure and function of metal-organic frameworks via linker design. Chem. Soc. Rev., 43: 5561-5593.

99. Szeto KC, Lillerud KP, Tilset M et al (2006) A thermally stable Pt/Y-based metal-organic framework: Exploring the accessibility of the metal Centers with spectroscopic methods using H_2O, CH_3OH, and CH_3CN as probes. J. Phys. Chem. B, 110: 21509-21520.
100. Szeto KC, Prestipino C, Lamberti C et al (2007) Characterization of a new porous Pt-containing metal-organic framework containing potentially catalytically active sites: Local electronic structure at the metal centers. Chem. Mater., 19: 211-220.
101. Szeto KC, Kongshaug KO, Jakobsen S et al (2008) Design, synthesis and characterization of a Pt-Gd metal-organic framework containing potentially catalytically active sites. Dalton Trans., 2054-2060.
102. Kandiah M, Usseglio S, Svelle S et al (2010) Post-synthetic modification of the metal-organic framework compound UiO-66. J. Mater. Chem., 20: 9848-9851.
103. Øien S, Agostini G, Svelle S et al (2015) Probing Reactive Platinum Sites in UiO-67 Zirconium Metal-Organic Frameworks. Chem. Mat., 27: 1042-1056.
104. Kamegawa T, Sakai T, Matsuoka M et al (2005) Preparation and characterization of unique inorganic-organic hybrid mesoporous materials incorporating arenetricarbonyl complexes [-$C_6H_4M(CO)_3$-] (M = Cr, Mo). J. Am. Chem. Soc., 127: 16784-16785.
105. Kaye SS, Long JR (2008) Matrix isolation chemistry in a porous metal-organic framework: Photochemical substitutions of N_2 and H_2 in $Zn_4O[(\eta^6$-1,4-benzenedicarboxylate)$Cr(CO)_3]_3$. J. Am. Chem. Soc., 130: 806-807.
106. Chavan S, Vitillo JG, Uddin MJ et al (2010) Functionalization of UiO-66 Metal−Organic Framework and Highly Cross-Linked Polystyrene with $Cr(CO)_3$: In Situ Formation, Stability, and Photoreactivity. Chem. Mater., 22: 4602-4611.
107. Goto Y, Sato H, Shinkai S et al (2008) "Clickable" Metal-Organic Framework. J. Am. Chem. Soc., 130: 14354-14355.
108. Gadzikwa T, Farha OK, Malliakas CD et al (2009) Selective Bifunctional Modification of a Non-catenated Metal-Organic Framework Material via "Click" Chemistry. J. Am. Chem. Soc., 131: 13613-13615.
109. Morris W, Doonan CJ, Furukawa H et al (2008) Crystals as molecules: Postsynthesis covalent functionalization of zeolitic imidazolate frameworks. J. Am. Chem. Soc., 130: 12626-12627.
110. Savonnet M, Aguado S, Ravon U et al (2009) Solvent free base catalysis and transesterifiation over basic functionalised Metal-Organic Frameworks. Green Chem., 11: 1729-1732.
111. Tanabe KK, Wang ZQ, Cohen SM (2008) Systematic functionalization of a metal-organic framework via a postsynthetic modification approach. J. Am. Chem. Soc., 130: 8508-8517.
112. Garibay SJ, Cohen SM (2010) Isoreticular synthesis and modification of frameworks with the UiO-66 topology. Chem. Commun., 46: 7700-7702.
113. Doonan CJ, Morris W, Furukawa H et al (2009) Isoreticular Metalation of Metal-Organic Frameworks. J. Am. Chem. Soc., 131: 9492-9493.
114. Gadzikwa T, Farha OK, Mulfort KL et al (2009) A Zn-based, pillared paddlewheel MOF containing free carboxylic acids via covalent post-synthesis elaboration. Chem. Commun., 3720-3722.
115. Ingleson MJ, Barrio JP, Guilbaud JB et al (2008) Framework functionalisation triggers metal complex binding. Chem. Commun., 2680-2682.
116. Hong DY, Hwang YK, Serre C et al (2009) Porous Chromium Terephthalate MIL-101 with Coordinatively Unsaturated Sites: Surface Functionalization, Encapsulation, Sorption and Catalysis. Adv. Funct. Mater., 19: 1537-1552.
117. Hermes S, Schröter M-K, Schmid R et al (2005) Metal@MOF: Loading of Highly Porous Coordination Polymers Host Lattices by Metal Organic Chemical Vapor Deposition. Angew. Chem. Int. Ed., 44: 6237-6241.
118. Zhao H, Song H, Chou L (2012) Nickel nanoparticles supported on MOF-5: Synthesis and catalytic hydrogenation properties. Inorg. Chem. Commun., 15: 261-265.
119. Bordiga S, Groppo E, Agostini G et al (2013) Reactivity of surface species in heterogeneous catalysts probed by in situ x-ray absorption techniques. Chem. Rev., 113: 1736-1850.
120. Bonino F, Lamberti C, Chavan S et al (2013) Characterization of MOFs. 1. Combined Vibrational and Electronic Spectroscopies. In F. Llabres i Xamena and J. Gascon (eds), Metal Organic Frameworks as Heterogeneous Catalysts, The Royal Society of Chemistry, Cambridge, pp. 76-142.
121. Borfecchia E, Gianolio D, Agostini G et al (2013) Characterization of MOFs. 2. Long and Local Range Order Structural Determination of MOFs by Combining EXAFS and Diffraction Techniques. In F. Llabres i Xamena and J. Gascon (eds), Metal Organic Frameworks as Heterogeneous Catalysts, The Royal Society of Chemistry, Cambridge, pp. 143-208.
122. Dietzel PDC, Panella B, Hirscher M et al (2006) Hydrogen adsorption in a nickel based coordination polymer with open metal sites in the cylindrical cavities of the desolvated framework. Chem. Commun., 959-961.
123. Chavan S, Bonino F, Vitillo JG et al (2009) Response of CPO-27-Ni towards CO, N_2 and C_2H_4. Phys. Chem. Chem. Phys., 11: 9811-9822.

124. Valenzano L, Vitillo JG, Chavan S et al (2012) Structure-activity relationships of simple molecules adsorbed on CPO-27-Ni metal-organic framework: In situ experiments vs. theory. Catal. Today, 182: 67-79.
125. Chavan S, Vitillo JG, Groppo E et al (2009) CO Adsorption on CPO-27-Ni Coordination Polymer: Spectroscopic Features and Interaction Energy. J. Phys. Chem. C, 113: 3292-3299.
126. Bonino F, Chavan S, Vitillo JG et al (2008) Local structure of CPO-27-Ni metallorganic framework upon dehydration and coordination of NO. Chem. Mater., 20: 4957-4968.
127. Diakun GP (1990) EXAFS - a Probe for Metalloproteins. Nature, 344: 83-84.
128. Strange RW, Ellis M, Hasnain SS (2005) Atomic resolution crystallography and XAFS. Coord. Chem. Rev., 249: 197-208.
129. Le Toquin R, Paulus W, Cousson A et al (2006) Time-resolved in situ studies of oxygen intercalation into $SrCoO_{2.5}$, performed by neutron diffraction and X-ray absorption spectroscopy. J. Am. Chem. Soc., 128: 13161-13174.
130. Piovano A, Agostini G, Frenkel AI et al (2011) Time Resolved in Situ XAFS Study of the Electrochemical Oxygen Intercalation in $SrFeO_{2.5}$ Brownmillerite Structure: Comparison with the Homologous $SrCoO_{2.5}$ System. J. Phys. Chem. C, 115: 1311-1322.
131. Mikkelsen JC, Boyce JB (1982) Atomic-Scale Structure of Random Solid Solutions: Extended X-Ray-Absorption Fine-Structure Study of $Ga_{1-x}In_xAs$. Phys. Rev. Lett., 49: 1412-1415.
132. Lamberti C (2004) The use of synchrotron radiation techniques in the characterization of strained semiconductor heterostructures and thin films. Surf. Sci. Rep., 53: 1-197.
133. Ankudinov AL, Ravel B, Rehr JJ et al (1998) Real-space multiple-scattering calculation and interpretation of x-ray-absorption near-edge structure. Phys. Rev. B, 58: 7565-7576.
134. Rehr JJ, Albers RC (2000) Theoretical approaches to x-ray absorption fine structure. Rev. Mod. Phys., 72: 621-654.
135. Filipponi A, Di Cicco A, Natoli CR (1995) X-ray-absorption spectroscopy and n-body distribution functions in condensed matter .1. Theory. Phys. Rev. B, 52: 15122-15134.
136. Filipponi A, Di Cicco A (1995) X-ray-absorption spectroscopy and n-body distribution functions in condensed matter .2. Data analysis and applications. Phys. Rev. B, 52: 15135-15149.
137. Rehr JJ, Ankudinov AL (2005) Progress in the theory and interpretation of XANES. Coord. Chem. Rev., 249: 131-140.
138. Benfatto M, Della Longa S (2001) Geometrical fitting of experimental XANES spectra by a full multiple-scattering procedure. J. Synchrot. Radiat., 8: 1087-1094.
139. Benfatto M, Della Longa S, Natoli CR (2003) The MXAN procedure: a new method for analysing the XANES spectra of metalloproteins to obtain structural quantitative information. J. Synchrot. Radiat., 10: 51-57.
140. Joly Y (2001) X-ray absorption near-edge structure calculations beyond the muffin-tin approximation. Phys. Rev. B, 63: art. no. 125120.
141. Guda SA, Guda AA, Soldatov MA et al (2015) Optimized Finite Difference Method for the Full-Potential XANES Simulations: Application to Molecular Adsorption Geometries in MOFs and Metal–Ligand Intersystem Crossing Transients. J. Chem. Theory Comput., 11: 4512-4521.
142. Kotani A, Shin S (2001) Resonant inelastic x-ray scattering spectra for electrons in solids. Rev. Mod. Phys., 73: 203-246.
143. Glatzel P, Bergmann U (2005) High resolution 1s core hole X-ray spectroscopy in 3d transition metal complexes - electronic and structural information. Coord. Chem. Rev., 249: 65-95.
144. Singh J, Lamberti C, van Bokhoven JA (2010) Advanced X-ray absorption and emission spectroscopy: in situ catalytic studies. Chem. Soc. Rev., 39: 4754-4766.
145. Swarbrick JC, Kvashnin Y, Schulte K et al (2010) Ligand Identification in Titanium Complexes Using X-ray Valence-to-Core Emission Spectroscopy. Inorg. Chem., 49: 8323-8332.
146. Gallo E, Lamberti C, Glatzel P (2011) Investigation of the valence electronic states of Ti(IV) in Ti silicalite-1 coupling X-ray emission spectroscopy and density functional calculations. Phys. Chem. Chem. Phys., 13: 19409-19419.
147. Gallo E, Bonino F, Swarbrick JC et al (2013) Preference towards Five-Coordination in Ti Silicalite-1 upon Molecular Adsorption. ChemPhysChem, 14: 79-83.
148. Mino L, Agostini G, Borfecchia E et al (2013) Low-dimensional systems investigated by x-ray absorption spectroscopy: a selection of 2D, 1D and 0D cases. J. Phys. D-Appl. Phys., 46: 72.
149. Giordanino F, Borfecchia E, Lomachenko KA et al (2014) Interaction of NH3 with Cu-SSZ-13 Catalyst: A Complementary FTIR, XANES, and XES Study. J. Phys. Chem. Lett., 5: 1552-1559.
150. Gallo E, Piovano A, Marini C et al (2014) Architecture of the Ti(IV) Sites in TiAlPO-5 Determined Using Ti K-Edge X-ray Absorption and X-ray Emission Spectroscopies. J. Phys. Chem. C, 118: 11745-11751.
151. Borfecchia E, Lomachenko KA, Giordanino F et al (2015) Revisiting the nature of Cu sites in the activated Cu-SSZ-13 catalyst for SCR reaction. Chem. Sci., 6: 548-563.
152. Groppo E, Gallo E, Seenivasan K et al (2015) XAS and XES Techniques Shed Light on the Dark Side of Ziegler-Natta Catalysts: Active-Site Generation. ChemCatChem, 7: 1432-1437.

153. Groppo E, Seenivasan K, Gallo E et al (2015) Activation and In Situ Ethylene Polymerization on Silica-Supported Ziegler–Natta Catalysts. ACS Catal., 5: 5586-5595.
154. Glatzel P, Alonso-Mori R, Sokaras D (2016) Hard X-ray Photon-in/Photon-out Spectroscopy: Instrumentation, Theory and Applications. In J. A. van Bokhoven and C. Lamberti (eds), X-Ray Absorption and X-Ray Emission Spectroscopy: Theory and Applications, John Wiley & Sons, Chichester, pp. 125-153.
155. Prestipino C, Regli L, Vitillo JG et al (2006) Local structure of framework Cu(II) in HKUST-1 metallorganic framework: Spectroscopic characterization upon activation and interaction with adsorbates. Chem. Mater., 18: 1337-1346.
156. Hafizovic J, Bjorgen M, Olsbye U et al (2007) The inconsistency in adsorption properties and powder XRD data of MOF-5 is rationalized by framework interpenetration and the presence of organic and inorganic species in the nanocavities. J. Am. Chem. Soc., 129: 3612-3620.
157. Masciocchi N, Galli S, Colombo V et al (2010) Cubic Octanuclear Ni(II) Clusters in Highly Porous Polypyrazolyl-Based Materials. J. Am. Chem. Soc., 132: 7902-7904.
158. Borfecchia E, Maurelli S, Gianolio D et al (2012) Insights into Adsorption of NH_3 on HKUST-1 Metal-Organic Framework: A Multitechnique Approach. J. Phys. Chem. C, 116: 19839-19850.
159. Mino L, Colombo V, Vitillo JG et al (2012) Spectroscopic and adsorptive studies of a thermally robust pyrazolato-based PCP. Dalton Trans., 41: 4012-4019.
160. Gallo E, Lamberti C, Glatzel P (2013) dd excitations in CPO-27-Ni metal-organic framework: comparison between resonant inelastic X-ray scattering and UV-vis spectroscopy. Inorg. Chem., 52: 5633-5635.
161. Shearer GC, Chavan S, Ethiraj J et al (2014) Tuned to Perfection: Ironing Out the Defects in Metal-Organic Framework UiO-66. Chem. Mat., 26: 4068-4071.
162. Jakobsen S, Gianolio D, Wragg DS et al (2012) Structural determination of a highly stable metal-organic framework with possible application to interim radioactive waste scavenging: Hf-UiO-66. Phys. Rev. B, 86: Art. n. 125429.
163. Milanesio M, Artioli G, Gualtieri AF et al (2003) Template burning inside TS-1 and Fe-MFI molecular sieves: An in situ XRPD study. J. Am. Chem. Soc., 125: 14549-14558.
164. Agostini G, Lamberti C, Palin L et al (2010) In Situ XAS and XRPD Parametric Rietveld Refinement To Understand Dealumination of Y Zeolite Catalyst. J. Am. Chem. Soc., 132: 667-678.
165. Gianolio D, Vitillo JG, Civalleri B et al (2013) Combined study of structural properties on metal-organic frameworks with same topology but different linkers or metal. J. Phys.: Conf. Series, 430: Art. n. 012134.
166. Øien S, Wragg D, Reinsch H et al (2014) Detailed Structure Analysis of Atomic Positions and Defects in Zirconium Metal-Organic Frameworks. Cryst. Growth Des., 14: 5370-5372.
167. Crabtree RH (1995) Aspects of Methane Chemistry. Chem. Rev., 95: 987-1007.
168. Arakawa H, Aresta M, Armor JN et al (2001) Catalysis research of relevance to carbon management: Progress, challenges, and opportunities. Chem. Rev., 101: 953-996.
169. Shilov AE, Shul'pin GB (1997) Activation of C-H bonds by metal complexes. Chem. Rev., 97: 2879-2932.
170. Labinger JA, Bercaw JE (2002) Understanding and exploiting C-H bond activation. Nature, 417: 507-514.
171. Lersch M, Tilset M (2005) Mechanistic aspects of C-H activation by Pt complexes. Chem. Rev., 105: 2471-2526.
172. Periana RA, Taube DJ, Gamble S et al (1998) Platinum catalysts for the high-yield oxidation of methane to a methanol derivative. Science, 280: 560-564.
173. Wolf D (1998) High yields of methanol from methane by C-H bond activation at low temperatures. Angew. Chem.-Int. Edit., 37: 3351-3353.
174. Palkovits R, Antonietti M, Kuhn P et al (2009) Solid Catalysts for the Selective Low-Temperature Oxidation of Methane to Methanol. Angew. Chem.-Int. Edit., 48: 6909-6912.
175. Palkovits R, von Malotki C, Baumgarten M et al (2010) Development of Molecular and Solid Catalysts for the Direct Low-Temperature Oxidation of Methane to Methanol. ChemSusChem, 3: 277-282.
176. Soorholtz M, White RJ, Zimmermann T et al (2013) Direct methane oxidation over Pt-modified nitrogen-doped carbons. Chem. Commun., 49: 240-242.
177. Stinton GW, Evans JSO (2007) Parametric Rietveld refinement. J. Appl. Crystallogr., 40: 87-95.
178. Bunker G, *Introduction to XAFS A Practical Guide to X-ray Absorption Fine Structure Spectroscopy*, Cambridge University Press, Cambridge, 2010.
179. Hall MD, Foran GJ, Zhang M et al (2003) XANES determination of the platinum oxidation state distribution in cancer cells treated with platinum(IV) anticancer agents. J. Am. Chem. Soc., 125: 7524-7525.
180. Yoshida H, Nonoyama S, Yazawa Y et al (2005) Quantitative determination of platinum oxidation state by XANES analysis. Phys. Scr., T115: 813-815.
181. Borfecchia E, Øien D, Svelle S et al (2015) A XAS study of the local environment and reactivity of Pt-sites in functionalized UiO-67 MOFs. J. Phys: Conf. Series, submitted.
182. Chui SSY, Lo SMF, Charmant JPH et al (1999) A chemically functionalizable nanoporous material $Cu_3TMA_2(H_2O)_{3n}$. Science, 283: 1148-1150.

183. Bordiga S, Regli L, Bonino F et al (2007) Adsorption properties of HKUST-1 toward hydrogen and other small molecules monitored by IR. Phys. Chem. Chem. Phys., 9: 2676-2685.
184. Smolentsev G, Soldatov A (2006) Quantitative local structure refinement from XANES: multi-dimensional interpolation approach. J. Synchrot. Radiat., 13: 19-29.
185. Groppo E, Prestipino C, Lamberti C et al (2003) Growth of NiO on Ag(001): Atomic environment, strain, and interface relaxations studied by polarization dependent extended X-ray absorption fine structure. J. Phys. Chem. B, 107: 4597-4606.
186. Humphrey SM, Allan PK, Oungoulian SE et al (2009) Metal-organophosphine and metal-organophosphonium frameworks with layered honeycomb-like structures. Dalton Trans., 2298-2305.
187. Nunez AJ, Shear LN, Dahal N et al (2011) A coordination polymer of (Ph_3P)AuCl prepared by post-synthetic modification and its application in 1-hexene/n-hexane separation. Chem. Commun., 47: 11855-11857.
188. Tan X, Li L, Zhang JY et al (2012) Three-Dimensional Phosphine Metal-Organic Frameworks Assembled from Cu(I) and Pyridyl Diphosphine. Chem. Mat., 24: 480-485.
189. Falkowski JM, Sawano T, Zhang T et al (2014) Privileged Phosphine-Based Metal-Organic Frameworks for Broad-Scope Asymmetric Catalysis. J. Am. Chem. Soc., 136: 5213-5216.
190. Morel FL, Ranocchiari M, van Bokhoven JA (2014) Synthesis and Characterization of Phosphine-Functionalized Metal-Organic Frameworks Based on MOF-5 and MIL-101 Topologies. Ind. Eng. Chem. Res., 53: 9120-9127.
191. Morel FL, Pin S, Huthwelker T et al (2015) Phosphine and phosphine oxide groups in metal-organic frameworks detected by P K-edge XAS. Phys. Chem. Chem. Phys., 17: 3326-3331.
192. Goesten MG, Gupta K, Ramos-Fernandez EV et al (2012) Chloromethylation as a functionalisation pathway for metal-organic frameworks. Crystengcomm, 14: 4109-4111.
193. Ranocchiari M, van Bokhoven JA (2013) Synthesis and Reactivity of Zn-Biphenyl Metal-Organic Frameworks, Introducing a Diphenylphosphino Functional Group. Chimia, 67: 397-402.
194. Vaclavik J, Servalli M, Lothschutz C et al (2013) AuI Catalysis on a Coordination Polymer: A Solid Porous Ligand with Free Phosphine Sites. ChemCatChem, 5: 692-696.
195. Engemann C, Franke R, Hormes J et al (1999) X-ray absorption near-edge spectroscopy (XANES) at the phosphorus K-edge of triorganophosphinechalcogenides. Chem. Phys., 243: 61-75.
196. Norman D (1986) X-ray absorption-spectroscopy (EXAFS and XANES) at surfaces. J. Phys. C-Solid State Phys., 19: 3273-3311.
197. Durham PJ (1988) Theory of XANES. In D. C. Koningsberger and R. Prins (eds), X-Ray Absorption: Principles, Applications, Techniques of EXAFS, SEXAFS and XANES, John Wiley & Sons, New York, pp. 53-84.
198. Bianconi A (1988) XANES spectroscopy. In D. C. Koningsberger and R. Prins (eds), X-Ray Absorption: Principles, Applications, Techniques of EXAFS, SEXAFS and XANES, John Wiley & Sons, New York, pp. 573-662.
199. Bianconi A, Garcia J, Benfatto M (1988) XANES in Condensed Systems. Top. Curr. Chem., 145: 29-67.
200. Kosugi N (1996) Theory and analysis of XANES: MO approach. In Yasuhiro Iwasawa (ed), X-ray absorption fine structure for catalysts and surfaces, World Scientific, Singapore, pp. 60-76.
201. Joly Y, Cabaret D, Renevier H et al (1999) Electron population analysis by full-potential X-ray absorption simulations. Phys. Rev. Lett., 82: 2398-2401.
202. Rehr JJ, Ankudinov AL (2001) Progress and challenges in the theory and interpretation of X-ray spectra. J. Synchrot. Radiat., 8: 61-65.
203. Yamamoto T (2008) Assignment of pre-edge peaks in K-edge x-ray absorption spectra of 3d transition metal compounds: electric dipole or quadrupole? X-Ray Spectrom., 37: 572-584.
204. Kas JJ, Jorissen K, Rehr JJ (2016) Real-Space Multiple-Scattering Theory of X-ray Spectra. In J. A. van Bokhoven and C. Lamberti (eds), X-Ray Absorption and X-Ray Emission Spectroscopy: Theory and Applications, John Wiley & Sons, Chichester, pp. 51-72.
205. Joly Y, Grenier S (2016) Theory of X-ray Absorption Near Edge Structure. In J. A. van Bokhoven and C. Lamberti (eds), X-Ray Absorption and X-Ray Emission Spectroscopy: Theory and Applications, John Wiley & Sons, Chichester, pp. 73-96.
206. Garino C, Borfecchia E, Gobetto R et al (2014) Determination of the electronic and structural configuration of coordination compounds by synchrotron-radiation techniques. Coord. Chem. Rev., 277: 130-186.
207. Bugaev LA, Gegusin, II, Datsyuk VN et al (1986) Multiple-Scattering Approach to the Xanes Theory of Alkali-Halide Crystals .1. Crystalline Potential in the X-Ray Absorption-Spectra Problem. Phys. Status Solidi B-Basic Res., 133: 195-202.
208. Bianconi A, Garcia J, Benfatto M et al (1991) Multielectron Excitations in the K-Edge X-Ray-Absorption near-Edge Spectra of V, Cr, and Mn 3d0 Compounds with Tetrahedral Coordination. Phys. Rev. B, 43: 6885-6892.
209. Tyson TA, Hodgson KO, Natoli CR et al (1992) General Multiple-Scattering Scheme for the Computation and Interpretation of X-Ray-Absorption Fine-Structure in Atomic Clusters with Applications to SF_6, $GeCl_4$, and Br_2 Molecules. Phys. Rev. B, 46: 5997-6019.

210. Chavan S, Bonino F, Valenzano L et al (2013) Fundamental Aspects of H_2S Adsorption on CPO-27-Ni. J. Phys. Chem. C, 117: 15615-15622.